Revealing the Structure of a Pre-Transitional Disk: The Case of the Herbig F Star SAO 206462 (HD 135344B)

M. Silverstone – Eureka Scientific
et al.

Citation of published version:

Grady, C.A., et al. (2009): Revealing the Structure of a Pre-Transitional Disk: The Case of the Herbig F Star SAO 206462 (HD 135344B). *The Astronomical Journal,* 699(2).
DOI: http://dx.doi.org/10.1088/0004-637X/699/2/1822

The Astrophysical Journal, 699:1822–1842, 2009 July 10 doi:10.1088/0004-637X/699/2/1822

REVEALING THE STRUCTURE OF A PRE-TRANSITIONAL DISK: THE CASE OF THE HERBIG F STAR SAO 206462 (HD 135344B)[a,b,c,d,e,f]

C. A. Grady[1,2,3], G. Schneider[4], M. L. Sitko[5,6,19], G. M. Williger[7,8,9], K. Hamaguchi[10,11,3], S. D. Brittain[12], K. Ablordeppey[6], D. Apai[4], L. Beerman[6], W. J. Carpenter[6], K. A. Collins[7,20], M. Fukagawa[13], H. B. Hammel[5,19], Th. Henning[14], D. Hines[5], R. Kimes[6], D. K. Lynch[15,19], F. Ménard[16], R. Pearson[15,19], R. W. Russell[15,19], M. Silverstone[1], P. S. Smith[4], M. Troutman[12,21], D. Wilner[17], B. Woodgate[18,3], and M. Clampin[18]

[1] Eureka Scientific, 2452 Delmer, Suite 100, Oakland, CA 96002, USA
[2] ExoPlanets and Stellar Astrophysics Laboratory, Code 667, Goddard Space Flight Center, Greenbelt, MD 20771, USA
[3] Goddard Center for Astrobiology, NASA Goddard Space Flight Center, Greenbelt, MD, USA
[4] Steward Observatory, The University of Arizona, Tucson, AZ 85721, USA
[5] Space Science Institute, 4750 Walnut Street, Suite 205, Boulder, CO 80301, USA
[6] Department of Physics, University of Cincinnati, Cincinnati, OH 45221-0011, USA
[7] Department of Physics, University of Louisville, Louisville, KY 40292, USA
[8] Department of Physics and Astronomy, John Hopkins University, Baltimore, MD 21218-2686, USA
[9] Department of Physics, The Catholic University of America, Washington, DC 20064, USA
[10] CRESST, X-Ray Astrophysics Laboratory, NASA/GSFC, Greenbelt, MD 20771, USA
[11] Department of Physics, University of Maryland, Baltimore County, 1000 Hilltop Circle, Baltimore, MD 21250, USA
[12] Department of Physics and Astronomy, Clemson University, Clemson, SC 29634-0978, USA
[13] Department of Earth and Space Science, Graduate School of Science, Osaka University, 1-1 Machikaneyama-cho, Toyonaka-shi, Osaka 560-0043, Japan
[14] Max-Planck-Institut für Astronomie, Königstuhl 17, D-69117 Heidelberg, Germany
[15] The Aerospace Corporation, Los Angeles, CA 90009, USA
[16] Laboratoire d'Astrophysique de Grenoble, CNRS/UJF UMR 5571, France
[17] Harvard-Smithsonian Center for Astrophysics, MS 42, 60 Garden Street, Cambridge, MA 02138, USA
[18] ExoPlanets and Stellar Astrophysics Laboratory, NASA's Goddard Space Flight Center, Greenbelt, MD 20771, USA
Received 2009 January 8; accepted 2009 April 27; published 2009 June 26

ABSTRACT

SAO 206462 (HD 135344B) has previously been identified as a Herbig F star with a circumstellar disk with a dip in its infrared excess near 10 μm. In combination with a low accretion rate estimated from Br γ, it may represent a gapped, but otherwise primordial or "pre-transitional" disk. We test this hypothesis with *Hubble Space Telescope* coronagraphic imagery, FUV spectroscopy and imagery and archival X-ray data, and spectral energy distribution (SED) modeling constrained by the observed system inclination, disk outer radius, and outer disk radial surface brightness (SB) profile using the Whitney Monte Carlo Radiative Transfer Code. The essentially face-on ($i \lesssim 20°$) disk is detected in scattered light from 0.″4 to 1.″15 (56–160 AU), with a steep ($r^{-9.6}$) radial SB profile from 0.″6 to 0.″93. Fitting the SB data requires a concave upward or anti-flared outer disk, indicating substantial dust grain growth and settling by 8 ± 4 Myr. The warm dust component is significantly variable in near to mid-IR excess and in temperature. At its warmest, it appears confined to a narrow belt from 0.08 to 0.2 AU. The steep SED for this dust component is consistent with grains with $a \leqslant 2.5$ μm. For cosmic carbon to silicate dust composition, conspicuous 10 μm silicate emission would be expected and is not observed. This may indicate an elevated carbon to silicate ratio for the warm dust, which is not required to fit the outer disk. At its coolest, the warm dust can be fit with a disk from 0.14 to 0.31 AU, but with a higher inclination than either the outer disk or the gaseous disk, providing confirmation of the high inclination inferred from mid-IR interferometry. In tandem, the compositional and inclination difference between the warm dust and the outer dust disk suggests that the warm dust may be of second-generation origin, rather than a remnant of a primordial disk component. With its near face-on inclination, SAO 206462's disk is a prime location for planet searches.

Key words: planetary systems: protoplanetary disks – stars: individual (SAO 206462)

[a] Based on observations made with the NASA/ESA *Hubble Space Telescope*, which is operated by the Association of Universities for Research in Astronomy, Inc., under NASA contract NAS5-26555.
[b] Based on observations made with the NASA-CNES-CSA *Far Ultraviolet Spectroscopic Explorer*. *FUSE* is operated for NASA by the Johns Hopkins University under NASA contract NAS5-32985.
[c] This work is based in part on observations made with the *Spitzer Space Telescope*, which is operated by the Jet Propulsion Laboratory, California Institute of Technology under a contract with NASA.
[d] This work is based in part on observations made with the NASA Infrared Telescope Facility, which is operated by the University of Hawaii under a contract with NASA.
[e] Based on observations obtained at the Gemini Observatory, which is operated by the Association of Universities for Research in Astronomy, Inc., under a cooperative agreement with the NSF on behalf of the Gemini partnership: the National Science Foundation (US), the Science and Technology Facilities Council (UK), the National Research Council (Canada), CONICYT (Chile), the Australian Research Council (Australia), Ministrio da Cincia e Tecnologia (Brazil), and SECYT (Argentina).
[f] Based in part on data collected at Subaru Telescope, which is operated by the National Astronomical Observatory of Japan.
[19] Visiting Astronomer, NASA Infrared Telescope Facility, operated by the University of Hawaii under contract to NASA.
[20] Supported by the Kentucky Space Grant Consortium and NASA.
[21] Michelson Fellow.

1. INTRODUCTION

One of the defining characteristics of a circumstellar disk is the excess emission above the photospheric light which becomes conspicuous in the spectrum at $\lambda \geqslant 1$ μm. The wavelength dependence of this IR spectral energy distribution (SED) has been used to infer the degree of dust grain growth and settling in protoplanetary disks (e.g., Furlan et al. 2005; Meeus et al. 2001; Dullemond & Dominik 2004a, 2004b). More recently, the *Spitzer* mission has resulted in identification of disks with either warm dust deficits compared to the mean excess for their associations, suggesting inner cavities which are at least partially cleared of dust, or those with dust emission deficits which are more localized in temperature. In the hope that such SEDs indicate an evolutionary sequence in the transition from gas-rich primordial disks to gas-poor debris disks, the warm *dust* deficit disks have been termed "transitional" disks (Strom et al. 1989) while the systems with dust deficits restricted to a smaller range in temperature have been termed either "gapped" or "pre-transitional" disks (Najita et al. 2007; Brown et al. 2007). Such terminology implicitly assumes that the warm and cold dust components are primordial, have the same composition, modulo sublimation effects as a function of radius, and share a common inclination with the gas disk.

Unfortunately, the SEDs of a disk where small grains are well mixed with the gas and a disk with a central cavity are similar, and cannot be distinguished based solely on modeling of the IR integrated-light SED. Moreover, different combinations of dust size distributions, opacities, dust morphologies, disk inclinations geometries can produce similar SEDs (Thamm et al. 1994; Chiang & Goldreich 1997, 1999, and as demonstrated in the range of acceptable model fits for specific disks in Robitaille et al. 2007). The problem extends to interpretation of molecular gas emission profiles. High-inclination (e.g., edge-on) disks with missing or reduced high-velocity gas have similar CO emission profiles to low-inclination (e.g., face-on) disks with material extending to the dust sublimation radius. However, the degeneracies in such modeling efforts can be broken if there are additional constraints on the disk structure and viewing geometry. As a result, disks that are sufficiently close to be studied in detail with the current generation of interferometers and high-contrast imaging techniques provide a crucial check on our understanding of the thousands of disks for which we have only IR SED data.

One such disk is associated with the Herbig F star SAO 206462 (HD 135344B, F4V, $v \sin i = 69$ km s^{-1}, Dunkin et al. 1997a, 1997b; $B = 9.206$, $V = 8.708$, $J = 7.279$, $H = 6.589$, $K = 5.843$). The star is part of a visual binary with SAO 206463 (HD 135344A, A0V, $V = 7.9$, $J = 7.582$, $H = 7.582$, $K = 7.583$) lying $\approx 20\farcs8$ to the NNE of SAO 206462 (Coulson & Walther 1995; Baines et al. 2006). The Herbig star was identified as a pre-main sequence (PMS) object from *IRAS* photometry (Walker & Wolstencroft 1988; Oudmaijer et al. 1992; Sylvester et al. 1996), and has subsequently been studied extensively with *Infrared Space Observatory* (*ISO*; Meeus et al. 2001; Walker & Heinrichsen 2000; Acke & van den Ancker 2004), *Spitzer* (Sloan et al. 2005; Kessler-Silacci et al. 2006; Brown et al. 2007), with the Submillimeter Array (Pontoppidan et al. 2008), and with the Very Large Telescope Interferometer/Mid-Infrared Interferometric Instrument (VLTI/MIDI; Fedele et al. 2008). The disk is CO-rich (Dent et al. 2005), and contains $(2.8 \pm 1.3) \times 10^{-3}$ $M_\odot$ of gas and dust (Thi et al. 2001). The IR spectrum lacks conspicuous emission from warm silicates, with at best weak amorphous silicate emission at 18 μm (Meeus et al. 2001; Kessler-Silacci et al. 2006). Weak polycyclic aromatic hydrocarbon (PAH) emission is present (Meeus et al. 2001; Sloan et al. 2005; Geers et al. 2006), as is [O I] emission from the inner disk (van der Plas et al. 2008).

Despite the wealth of observations, many of the basic parameters of SAO 206462's disk have proven controversial, from the system inclination, with estimates in the literature ranging from 11° to 60° (Dent et al. 2005; Pontoppidan et al. 2008; Doucet et al. 2006; Fedele et al. 2008), the distance to the star (Coulson & Walther 1995; van Boekel et al. 2005), to whether SAO 206462 has a flared, protoplanetary disk or a pre-transitional disk (Meeus et al. 2001; Brown et al. 2007; Pontoppidan et al. 2008). We combine new and archival data to address both the outer and inner disk properties. *Hubble Space Telescope* (*HST*)/NICMOS coronagraphic imagery at 1.1 μm, supplemented by a re-analysis of archival *HST* coronagraphy for this star are used to address the outer disk inclination, radial surface brightness (SB) profile, and place limits on companions. *Far Ultraviolet Spectroscopic Explorer* (*FUSE*) FUV, *HST* Advanced Camera for Surveys (ACS) data and NIR spectroscopy and X-ray data are used to test the accretion rate estimate noted by Garcia Lopez et al. (2006). We combine these data with modeling of both literature and new IR observations to test the hypothesis that SAO 206462 is a pre-transitional disk.

2. OBSERVATIONS AND DATA REDUCTION

2.1. HST Coronagraphy

SAO 206462 has been coronagraphically imaged at three epochs by *HST*: in the NIR with NICMOS, at 1.1 and 1.6 μm, and once with Space Telescope Imaging Spectrograph (STIS) in broadband NUV–NIR light (Grady et al. 2005; Table 1).

2.1.1. NICMOS F110W Imagery

We conducted *HST*/NICMOS imaging of SAO 206462 on 2005 March 24 UT with NICMOS camera 2 as part of a larger coronagraphic survey of protoplanetary and young debris disks (HST-GO-10177, P.I.: G. Schneider). The observations of SAO 206462 were obtained at two celestial field orientations (spacecraft roll angles) separated by $29\fdg9$ obtained within a single orbit (visits 39 and 3A of HST-GO-10177). Each visit consisted of F171M target acquisition imaging (ACQ), deep coronagraphic (CORON) images obtained in the F110W ($\lambda_{\rm eff} = 1.104$ μm, FWHM $= 0.5915$ μm) filter, and following a $2\farcs83$ slew, direct-light imaging of the core-saturated unocculted (DIRECT) stellar point-spread function (PSF). The pixel scale for NICMOS camera 2 is $\sim$75.8 mas pixel^{-1}.

Calibration and data reduction followed Schneider et al. (2006). Our subsequent analysis of the coronagraphic imagery used both roll-differencing (Lowrance et al. 1999), an early and simplified version of what is now being termed active astrometric differential imaging and template PSF observation subtraction to separate scattered light originating in the disk and any faint companions from the residual stellar diffracted and instrumentally scattered light (Grady et al. 2007). Figure 1 shows the full $19\farcs2 \times 19\farcs3$ NICMOS image for the first of the two visits, together with the same data after roll-differencing. Template PSF observations were drawn from both dedicated PSF targets and objects with disk nondetections from program 10177. For template PSF observation subtraction, we register the template data to the location of our science target in each visit, and then scale the template data by the ratio of the stellar fluxes in the visit-contemporaneous unocculted

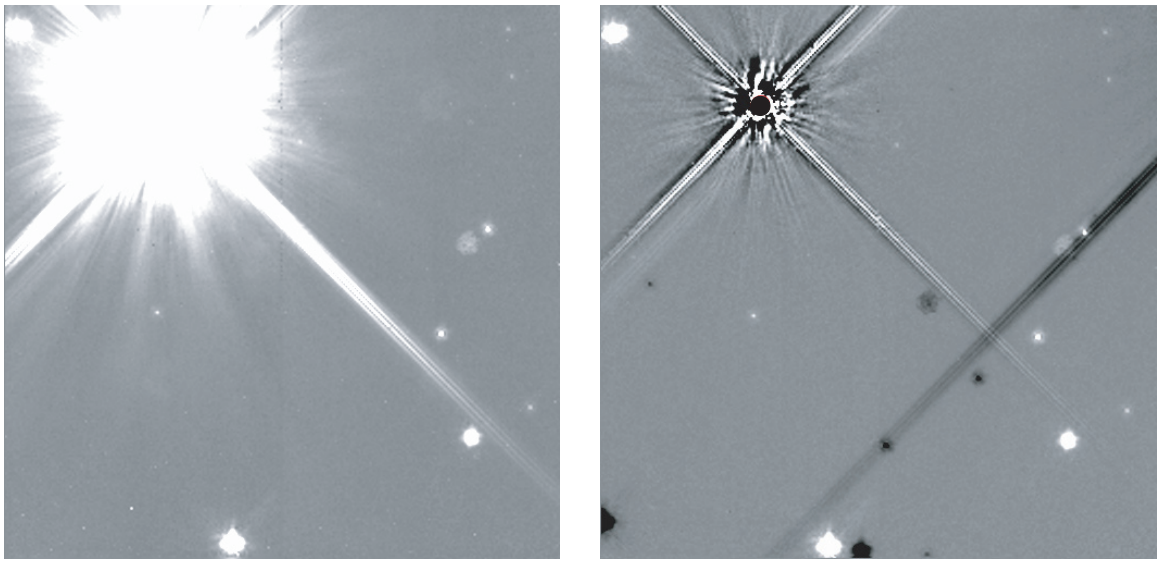

Figure 1. (a) Full 19.″2 ×19.″3 NICMOS F110W image for the first SAO 206462 visit. The image display dynamic range is ± 200 μJy arcsec^{-2}. (b) The same image after subtraction of the second visit data, shown with the same dynamic range as Figure 1(a). Features from the second visit are in negative. (The linear, negative feature to the lower right of SAO 206462 is a partial diffraction spike due to the 21″ distant SAO 206463, which lies beyond the NICMOS field of view).

Table 1
Journal of *HST* Coronagraphic Observations

Star	Type	Color[a]	Prog[b]	Inst.	Filter[c]	T_{exp} (s)[d]	Obs. ID[e]	Date
SAO 206462	F4Ve	0.44	10177	NIC	F110W	703.88	N8ZU39/3A	2005 Mar 24
HD 83870	G5V	0.29	10177	NIC	F110W	703.88	N8ZU61/62	2005 Feb 24
SAO 93101	K0V	0.43	10177	NIC	F110W	703.88	N8ZU3D/3E	2004 Dec 02
HD 84773	A2IIII		10177	NIC	F110W	703.88	N8ZU5D/5E	2004 Aug 29
SAO 206462	F4Ve	0.44	7857	NIC	F160W	783.50	N4NL01	1998 Aug 22
GL 693	M2V	0.56	7227	NIC	F160W	767.88	N4NF59	1998 Apr 30
SAO 206462	F4Ve	0.48	8674	STIS		1200	o65410010	2001 Apr 08
HD 134970	F5V	0.46	8674	STIS		1260	o65420010	2001 Apr 08
HR 4413	F7V	0.50	8925	STIS		84	o6I401040	2001 Aug 02
HR 3802	K4III	1.52	9136	STIS		64-65	o6BX47010-50	2001 Oct 13
HR 2662	K3III	1.40	9136	STIS		37	o6BX46010-70	2001 Oct 12

Notes.
[a] $J-H$ for NICMOS observations, $B-V$ for STIS.
[b] *HST* program identification number assigned by STScI.
[c] Filter for NICMOS coronagraphic imaging, preceded by F171M or F180M target acquisition, and followed in program 10177 by short (< 1 s) F110W direct, images.
[d] Total integration time for all exposures in each visit (no. exp = 3 for all except 7857/SAO 206462 with no. exp = 7).
[e] Root name for observation ID assigned by STScI. See STScI/MAST archive for additional observational details.

F110W images. Our initial selection of PSF template stars, chosen to be close in spectral type to SAO 206462 resulted in excess light detections, but with color-mismatch errors. Subsequently, we selected candidate PSF subtraction template stars with $J-H$ color indices similar to SAO 206462 that exhibited no intrinsic scattered-light excesses as determined from the GO 10177 survey data. Data for HD 83870, HD 93101, and HD 84773 had both reasonable color and *HST* focus ("breathing") residual matches to the SAO 206462 observations and were used as PSF template data, providing six science minus PSF template subtraction pairs. Excess light was detected in *all 12* of these subtractions for *both* SAO 206462 visits within 1.″05 of the star. The individual target minus template PSF subtractions were masked to exclude edge-artifacts due to the $r = 0.''3$ coronagraphic obscuration. The appearance of a frequently occurring coronagraphic image artifact (discussed in detail by G. Schneider et al. 2009, in preparation; Section 5.3), in the upper right quadrant close to the coronagraphic obscuration in that sector adversely affected that small portion of the SAO 206462 PSF subtracted images and could not be mitigated in two-roll combination due to its larger angular-azimuthal extent. Given the small angular scale of the circumstellar excess light distribution, diffraction spikes were not masked, but these were much fainter than the excess light near the star. The individual subtraction pairs from each SAO 206462 visit were separately combined. Next, the median-combined data for each visit were rotated to place north up and east to the left, prior to averaging (Figure 2(a)).

2.1.2. NICMOS F160W Imagery

SAO 206462 was observed in 1998 under HST-GO-7857 in tandem with SAO 206463 (HD 135344A, A0V, $J = H = K =$) which was used as the PSF template star by Augereau et al. (2001). SAO 206462 and SAO 206463 have Two Micron

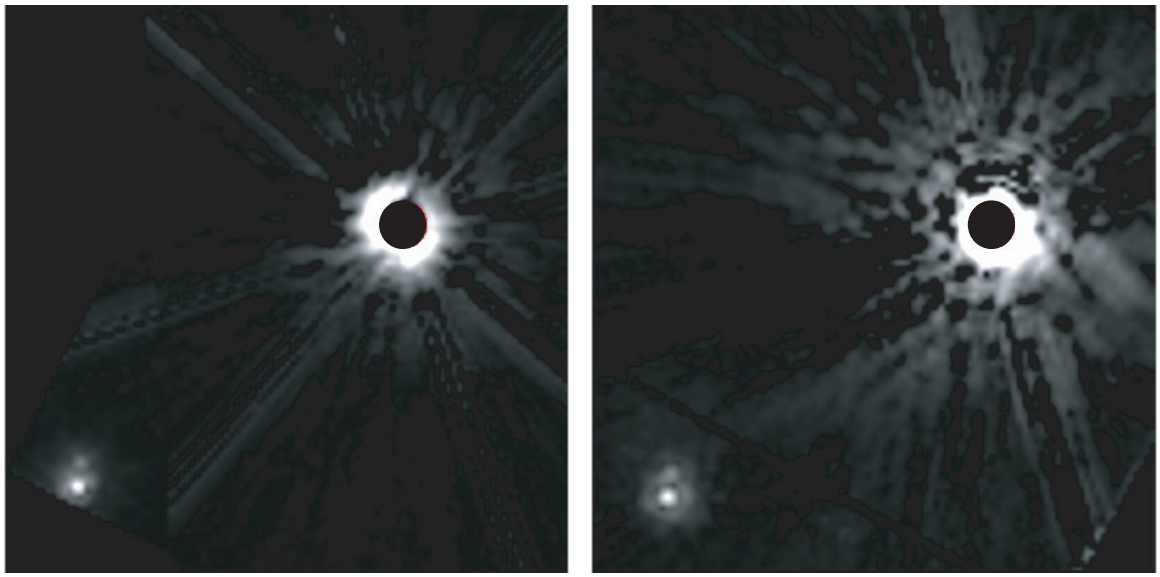

(a) (b)

Figure 2. Disk of SAO 206462 following PSF subtraction. Data from both spacecraft orientations are averaged to form these images. The image field of view is 7.″5 on a side, with north up and east to the left. The images are shown with a logarithmic stretch from 0.05 to 25 mJy arcsec^{-2}. The black circle indicates the location of the 0.″3 coronagraphic spot. (a) F110W from 2005 and (b) F160W from 1998. The apparent decrement in the 1.1 μm disk SB to the northwest of the star arises from a coronagraphic image artifact (see Section 2.1.1) and is not intrinsic to the disk. The binary star noted by Augereau et al. (2001) is in the lower left of each image and displays the reflex of SAO 206462's proper motion, demonstrating that it is a background object.

All Sky Survey (2MASS)-determined $H-K$ colors of 0.746 and 0.119, respectively. The color difference is sufficient to produce chromatic dispersion in the PSF subtraction residuals at a level capable of swamping the signal from the disk. We have re-analyzed the F160W observation of SAO 206462, after reprocessing the raw archival imagery retrieved from the Multimission Archive at STScI, using the best suited of the few contemporaneous and sufficiently bright coronagraphic stellar PSF templates available: GL 693 ($J = 6.855$, $H = 6.297$, $K = 6.016$, $H - K = 0.281$ from HST-GTO-7227, P.I.: G. Schneider). GL 693 differs in $J-H$ and $H-K$ from SAO 206462 by +0.134, and +0.463, a much better color match than SAO 206463 ($\Delta(J - H) = 0.692$, $\Delta(H - K) = 0.725$). SAO 206462 was observed by Augereau et al. (2001) at only a single field orientation, but GL 693 was observed at two, resulting in two PSF-subtracted images. While the target/template stars were still not optimized in color, after flux-density scaling and astrometric registration, the two PSF-subtracted images produced very similar scattered light excesses at $r \leqslant 0.''8$. At larger angular distances, the residual color-mismatch between the template star and SAO 206462 resulted in a small zonal undersubtraction of the PSF beyond 0.″8 in both science target—PSF template images. The F160W PSF-subtracted imagery were registered to the frame of the F110W imagery and were averaged (Figure 2(b)).

2.1.3. STIS Coronagraphic Imagery

SAO 206462 was observed in the broadband optical (0.2–1.0 μm) on 2001 April 8 as part of HST-GO-8674 with the STIS coronagraphic imaging mode along with a contemporary, spectral type-matched PSF star, HD 134970 (F5V, $V = 8.56$, $B = 9.02$, $B - V = 0.46$), and has previously been discussed by Grady et al. (2005) as a disk nondetection. The STIS coronagraph incompletely apodizes the stellar diffraction spikes produced by scattering off the *HST* secondary support structure, with the result that these features are typically the brightest residual features in observations of occulted stars. The diffraction spikes are used both to register PSF template observations to the science target data and to empirically derive the flux renormalization scale factor needed to null the diffraction spikes (Grady et al. 2005). The scale factor derived in this process is in good agreement with that predicted using the mean V of SAO 206462 and literature values for HD 134970. For a debris disk, this close a spectral type and color match results in a PSF subtraction dominated by temporal changes in the breathing residuals only. However, after subtracting the registered and scaled PSF template data, we find a residual image in both the diffraction spikes and off the spikes, suggesting that we have incompletely subtracted the stellar light. The excess light along the diffraction spikes can be nulled with the addition of a red PSF template (either HR 3802 or HR 2662) accounting for 3.4% of the integrated system light in the unfiltered STIS CCD bandpass (0.2–1.0 μm with $\lambda_{\rm eff} = 5875$ Å), at the expense of larger breathing residuals. We obtain similar results, but with even larger breathing residuals when HD 134970 is replaced by the STIS coronagraphic PSF library target HR 4413. These data suggest that SAO 206462 is redder than expected for a typical F4V-F8V star in the 0.2–1.0 μm range. We note that SAO 206462 has a strong near-IR excess: up to 20% of the flux at 1 μm is light contamination from the warm inner disk (Coulson & Walther 1995). However, after nulling the spikes using a linear combination of HD 134970 and a red PSF component, there is still residual light within 1.″15 of the star, which we now interpret, in view of the NICMOS data, as a scattered-light disk detection (Figure 3(a)). Unfortunately, the large size of the STIS coronagraphic wedge relative to the disk precludes more detailed analysis of the STIS data.

2.2. ACS SBC F122M Imagery

SAO 206462 was observed on 2007 May 19 with the ACS using the Solar Blind Channel (SBC) and the F122M filter (nominal $\lambda_{\rm eff} = 1210$ Å, FWHM = 60 Å) as part of HST-

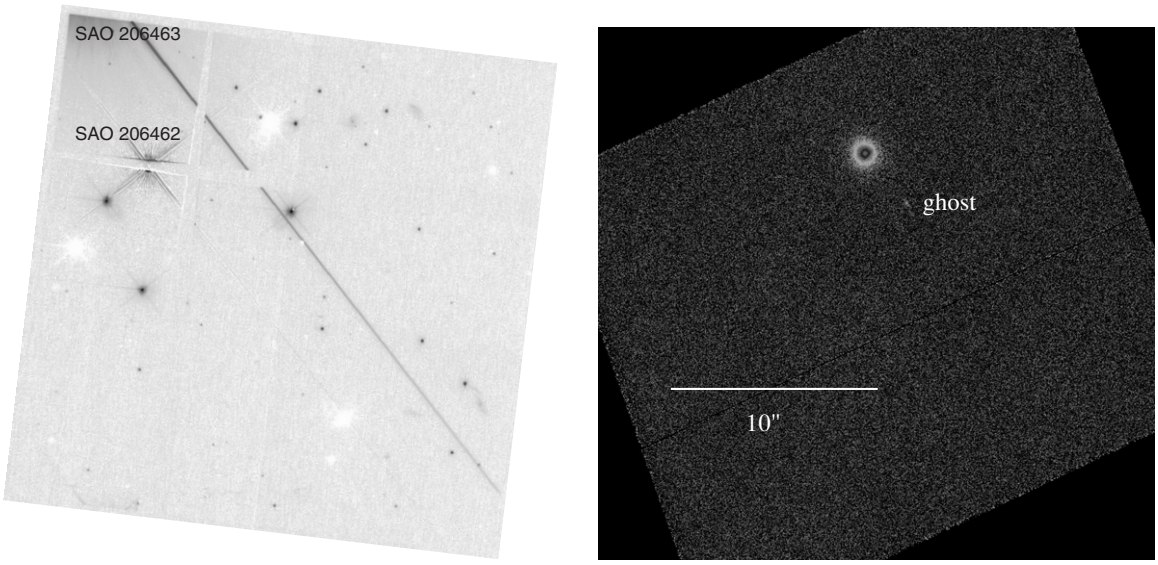

Figure 3. Field of SAO 206462 in the broadband optical and FUV. (a) SAO 206462 as seen following PSF subtraction by STIS in 2001. The field of view is 50″ on a side, and the image is oriented to place north up and east to the left. Residual light is marginally detected on either side of the coronagraphic wedge out to 1.″15, with some suggestion of asymmetry to the north of the star. The imperfect color match of the composite of HD 134970 + a red PSF component to the color of SAO 206462 is visible as residual tiger-striping on the diffraction spikes. (b) ACS SBC image of SAO 206462 shows only a single point source and the known filter ghost (Collins et al. 2007). The field of view includes the candidate binary companion noted by Augereau et al. (2001), but this source is not detected in the FUV, suggesting that it is a background object.

Table 2
Journal of *FUSE* FUV Spectra

Star	Sp.T.	d (pc)	$B-V$	Id.	Date	T_{exp} (s)
SAO 206462	F4Ve	84 or 140	0.48	Q3060201000	2003 Jun 9	8,444
HR 4796	A0V+M2V	67	0.00	B0910401000	2002 Apr 25	12,378
HD 139614	A7−8Ve	140	0.23	E5100501000	2004 Jul 17	31,998
MWC 480	A5Ve	131	0.17	E5100101000	2004 Oct 24	26,363

GO-10864. The ACS exposure, with a total integration time of 1624 s. was segmented into four subexposures within a single spacecraft orbit, with the subexposure pointings differentially offset ("dithered") using the ACS small-box dither pattern with dither offsets of ≈ 0.″15–0.″19. An offset aperture location was used to avoid placing SAO 206463 on the SBC detector. The data were processed using the default ACS pipeline software including geometric distortion correction and use of the multidrizzle algorithm to produce a co-added, geometric-distortion corrected image (Pavlovsky et al. 2006). In the final imagery, the image scale is 0.″025 pixel^{-1} (Figure 3(b)). The ACS F122M image, after pipeline processing has a background level of 1.03 ± 0.82 millicounts per pixel. One point source is detected, at the expected location for SAO 206462, together with the ACS SBC filter ghost (Collins et al. 2007). The exposure depth of this image is sufficient to detect weak T Tauri stars with spectral types as late as M2-M3V at $d = 140$ pc with signal-to-noise ratio, S/N ⩾ 3.

2.3. FUSE Spectrum

The *FUSE* observed several Herbig Ae stars, including SAO 206462, as well as a number of A-debris disks from 912 to 1186 Å (Table 2) at a spectral resolution of 20,000 using the default 30″ × 30″ LWRS aperture in the time-tag mode. The data for SAO 206462 were processed under CALFUSE 3.0.8, while our comparison stars HD 139614 and MWC 480 were processed using CALFUSE 3.0.7 (see Dixon et al. 2007). Long-duration *FUSE* observations, such as these, are typically made up of shorter integrations, given the low-earth orbit of the *FUSE* spacecraft. Individual spectral exposures were inspected and stacked using the CORRCAL routine written by S. Friedman. As is typical of Herbig stars in the FUV, the *FUSE* spectra of all three stars have emission in C III 977, 1176, and O VI 1032, 1038 Å. MWC 480 and SAO 206462 have weak continua (S/N ∼2) visible at the longest *FUSE* wavelengths, while HD 139614 has no detectable continuum despite a longer exposure duration (Figure 4). In addition to the C III and O VII emission, MWC 480 has emission in several Fe II transitions seen in other Herbig Ae stars. Harper et al. (2001) have noted that these transitions are pumped by Lyman α and originate near 1 AU. These features are not seen in the spectra of SAO 206462 or HD 139614. Martin-Zaïdi et al. (2008) find only an upper limit for N(H_2) in the line of sight to SAO 206462.

Contamination from HD 135344A. Given the size of the *FUSE* LWRS, and limitations on pointing stability during *FUSE* spectral exposures, we have assessed the extent of stray-light contamination of the SAO 206462 data by light from HD 135344A. Between 1100 and 1190 Å, typical A0V spectra are dominated by photospheric light, with the most conspicuous features the wing of H I Lyman α at the long-wavelength end of the spectrum, the C I absorption edge, and numerous saturated C I absorption features. Adopting HR 4796 A as a representative A0V star (see Gerbaldi et al. 1999 for the wide range in T_{eff} spanned by A0V), an unreddened A0V star scaled to $d = 140$ pc should produce a peak flux near 1130 Å of 4 ×

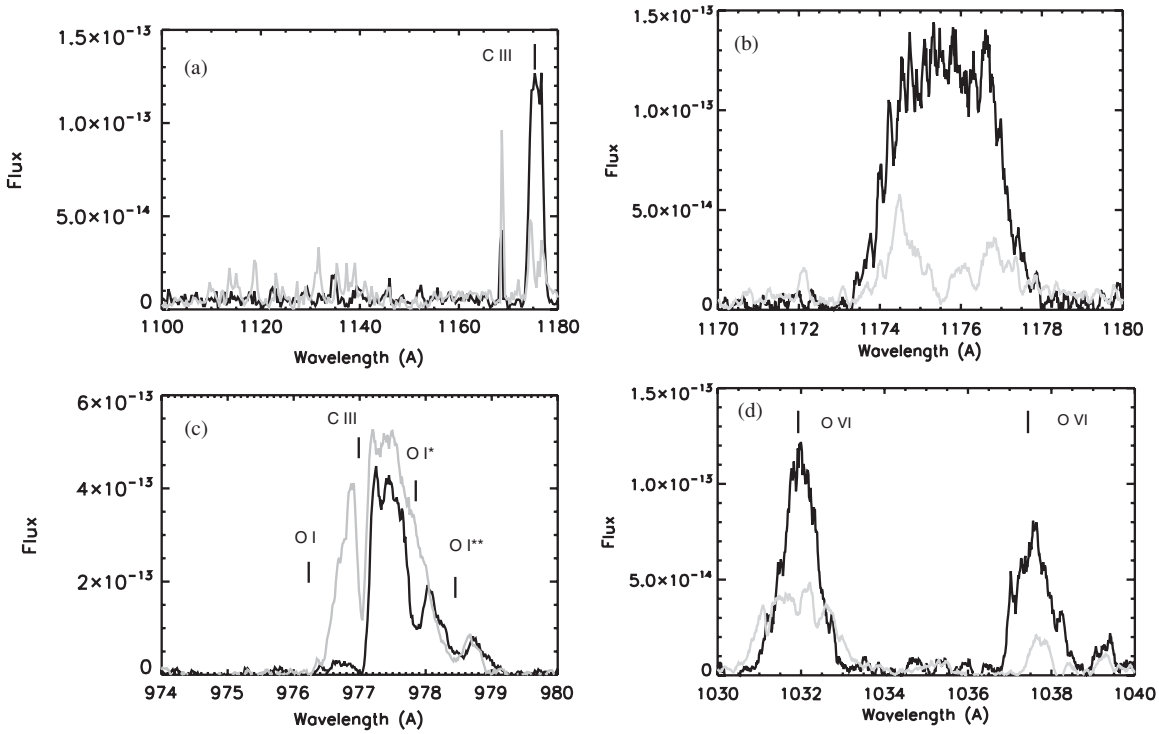

Figure 4. FUV data for SAO 206462 (black), and comparison stars HD 139614 and MWC 480. (a) A faint continuum is present in the spectra of MWC 480 (gray) and SAO 206462 from 1090 to 1180 Å. (b) The C III λ1176 profile for SAO 206462 has the blocky shape characteristic of chromospheric emission profiles rather than the double-peaked emission seen in MWC 480 (gray). (c) The C III λ977 profile, while chopped up by O I absorption has a type I P Cygni profile indicating the presence of a high velocity, moderate temperature wind similar to that observed by Dupree et al. (2005) in TW Hya. This wind is not seen in HD 139614 (gray). (d) The O VI profile for SAO 206462 is narrow compared to MWC 480 (gray) which is typical of the jet-driving Herbig Ae stars, but is broad compared to moderate $v \sin i$ transition region sources.

10^{-13} erg cm^{-2} s^{-1} Å^{-1} if entirely in the *FUSE* LWRS aperture. This would dominate the observed spectrum, and would also leave the imprint of both the photospheric Lyα absorption near 1180 Å and the C I absorption edge from 1110 to 1140 Å on the spectrum. An A0V reddened by foreground interstellar material following the Sasseen et al. (2002) extinction law would produce half this flux if fully in the LWRS aperture. This high a continuum flux level and the associated distinctive absorption lines are not detected (see Figure 4(a)). Shortward of 1120 Å, the continuum of a typical A0V star drops rapidly with decreasing wavelength, and with the same level of contamination would produce a continuum which is an order of magnitude fainter than the observed spectrum. From the lack of any discontinuity in the continuum across the C I edge, we conclude that the SAO 206462 spectrum has negligible contamination from HD 135344A and is intrinsic to the Herbig Fe star.

2.4. *ROSAT*

Young mid-F stars are expected to be X-ray sources (de la Reza & Pinzón 2004), and a source is detected at the 6.2σ level in a 4790.5 s *ROSAT* HRI pointed observation of the SAO 206462 field (Obs. ID: RH202086N00) obtained on 1996 February 11 (Figure 5). The source is offset 0.″89 from SAO 206462, consistent with the *ROSAT* pointing accuracy. This source has a count rate of 0.0104 ± 0.0017 counts s^{-1}, measured with the sosta tool of ximage. The count rate is 83% of the HRI count rate for the accreting Herbig Ae star HD 163296 (d = 122 pc; Skinner et al. 2004) and is similar to AK Sco (SB2 at d = 150 pc; Skinner et al. 2004). The *ROSAT* HRI has a known UV leak. Using Equations (1) and (2) in Berghöfer et al. (1999) and $U = 9.^{\rm m}6$ magnitude in Malfait et al. (1998), we estimate the contribution to the measured count rate of UV contamination to be $<5 \times 10^{-7}$ counts s^{-1}. The more UV-luminous HD 135344A was not detected in this

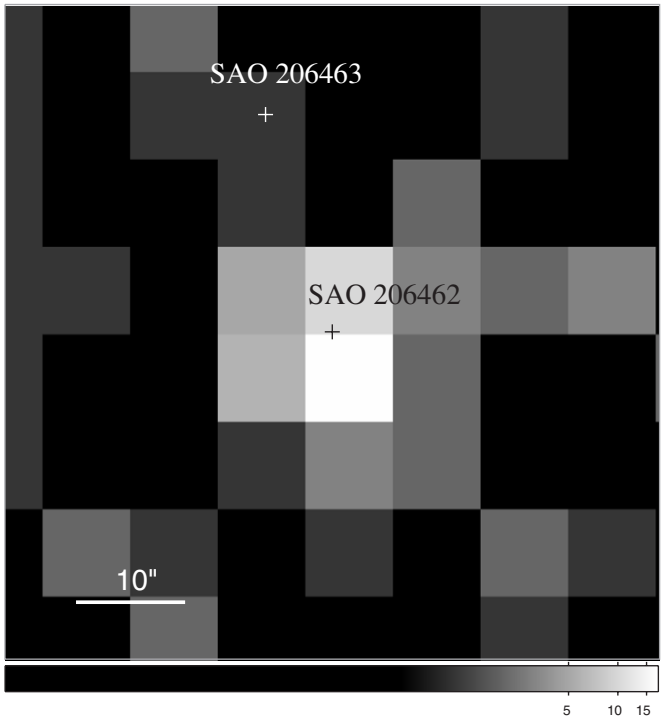

Figure 5. *ROSAT* HRI image of SAO 206462 and HD 135344A. HD 135344 A was not detected, as expected for a nonaccreting, young A0V star.

exposure, providing independent verification of negligible UV contamination of the X-ray data. No X-ray detection of HD 135344A, a nonaccreting ZAMS A star, was expected (see Stelzer et al. 2006). Assuming $kT = 0.3$ keV and $N_H = 0$ cm^{-2}, the X-ray flux for SAO 206462 is $F_X = 2 \times 10^{-13}$ erg cm^{-2} s^{-1}. For $d = 140$ pc this would correspond to $\log(L_X) = 29.66$, while at $d = 84$ pc, $\log(L_X) = 29.2$.

2.5. New Optical Observations with BASS CCD

Observations of SAO 206462 at 0.44 and 0.71 μm were obtained in 2006 August 5, using the Aerospace Corporation's Broadband Array Spectrograph System (BASS) guide camera and BC and RC "Hale–Bopp" filters (Farnham et al. 2000). These are intermediate-bandpass filters ($\delta\lambda \sim 0.006$ μm) normally used to isolate the light scattered by cometary dust grains, but are useful for observing bright objects with large telescopes. The narrow bandpasses minimizes the need for color terms in the atmospheric extinction correction. The data on SAO 206462 were calibrated using HD 120086, a flux calibration star for the Hale–Bopp filter set. The scale of the CCD camera at the casegrain focus of the IRTF is 5.2 pixel arcsec^{-1}. For the data extraction, a circular aperture of 3.″4 was used, in order to match the aperture used for the infrared observations, and sky backgrounds determined using an annulus with inside and outside boundaries of 15″and 19″, respectively. The mean air masses for the observations were 2.26 and 1.90, respectively. Atmospheric extinction coefficients were determined using observations of HD 120086 (air mass 1.90) and another Hale–Bopp calibration standard star, HD 11131 (air mass 1.19). The SAO 206462 data were corrected to zero air mass using extinction coefficients of 0.18 mag per air mass for the BC observations and 0.10 mag per air mass for the RC observations.

2.6. New Infrared Data

2.6.1. BASS-IR

Observations were obtained of SAO 206462 using BASS with the IRTF in 2007 July 9 UT. Telluric corrections and flux calibration were performed using observations of α Lyr. The mean air masses for the observations of SAO 206462 and α Lyr were 1.89 and 1.77, respectively. The 3.″4 diameter circular entrance aperture allows for absolute fluxes to be determined, and these were used to normalize to normalize the SpeX data from the previous night 2007 July 8 in the 3–5 μm region where they overlap in wavelength (as discussed below). BASS-IR data reduction is described in Sitko et al. (2008). scatter in the individual multiple measurements indicated that the overall flux level of the BASS data (particularly at the shortest wavelengths) are uncertain by 5% due to variations in the seeing at the time of the observations.

2.6.2. SpeX

SAO 206462 was observed on 2007 May 1 (UT), 2007 July 8 (UT), and 2008 May 22 (UT) with the SpeX instrument (Rayner et al. 2000) on NASA's Infrared Telescope Facility. For 2007 May 1, two spectra were obtained using the echelle gratings and 0.″8 slit, one covering 0.8–2.4 μm (SXD mode) with an effective resolution of ∼750 and the other covering 2.3–5.4 μm (LXD2.3 mode) with an effective resolution of ∼950. Both observations were obtained under 0.″7 seeing. The data were corrected for atmospheric extinction and flux calibrated using the standard techniques (Vacca et al. 2003) using the Spextool software package (Cushing et al. 2004). The calibration star used was HD 129685 (A0V). The mean air masses for the observations of SAO 206462 and HD 129685 were 1.84 and 1.75, respectively.

For the July 8 data, the sky had considerable cirrus, and only SXD data were obtained. The data for SAO 206462 were flux calibrated against HD 129685 with air masses of 1.94 and 1.75, respectively. The zero point was determined using BASS observations made the following night, under clear skies but diminished seeing conditions. The mismatch of 0.2 in the air mass can lead to systematic errors (at the shorter wavelengths due to the anchoring of the long wavelength data to BASS), in this case making the shortest wavelength fluxes slightly low. The seeing during the BASS observations could potentially introduce a 5% shift as well.

On 2008 May 22, we obtained SXD, LXD as well as data using the prism disperser. For the LXD, the calibration star was HD 129685, and the mean air masses of the two stars were 2.22 and 2.06, respectively. The air mass match for SXD were poor—SAO 206462 being 2.31 and two separate observations of HD 129685 being 1.96 and 2.77. Using either observation independently would lead to a serious systematic error in the spectral shape. For the SXD observations we used a mean, weighted by the closeness of the air mass match between the two stars. The prism observations were obtained prior to the high-resolution observations, with a 3.″0 slit to maximize light throughput, and a good air mass match (1.86 versus 1.93). The flux levels obtained from the prism data agree to within a few percent with the weighted mean SXD data at the wavelengths where they overlap.

2.6.3. NICMOS Target Acquisition Photometry

As part of the coronagraphic observations, SAO 206462 was acquired by *HST*/NICMOS using 0.5 and 0.353 s F171M ($\lambda_{\rm center} = 1.721$ μm, FWHM = 0.0712 μm) images in both the 1998 (program 7857) and 2005 (program 10177) observations. The absolute flux density calibrations over this eight year baseline are accurate to ∼2%, largely due to quantum efficiency changes with temperature in 1998 (cycle 7) affecting the sensitivity calibration. Within the two 2005 (cycle 13) observations, which are separated by only 22 minutes, but come from independent target acquisitions, with the star placed at different locations on the NIC2 detector, the repeatability is at the 1% level. The variation from 1998 to 2005 is at 2.5σ over the relative photometric uncertainties. The 2005 NICMOS photometry is in good agreement with the 2MASS photometry from 2000 February 4.

2.6.4. Subaru Photometry

SAO 206462 was observed in J, L', and M' bands on 2008 July 11 with CIAO (Murakawa et al. 2004) at the Subaru Telescope. The sky was photometric and the poor seeing condition (∼1.″3) permitted the photometry to be unsaturated. The J-band images were obtained with a four position dither pattern, and a two position dithering was performed in L' and M'. In J band, eight data frames were taken with each exposure time of 5 s. In L' and M', 10 exposures of 0.33 and 0.18 s were co-added into one frame, and total 20 and 40 frames were obtained, respectively. The flat-fielding and sky subtraction for the L' and M' images were carried out using the pair of dithered images, while the twilight flat was employed for the flattening of the J-band data. The magnitudes were measured by aperture photometry, then calibrated using the standard stars FS 140 in J (Leggett et al. 2006), HD 129655 and HD 203856 in L' and

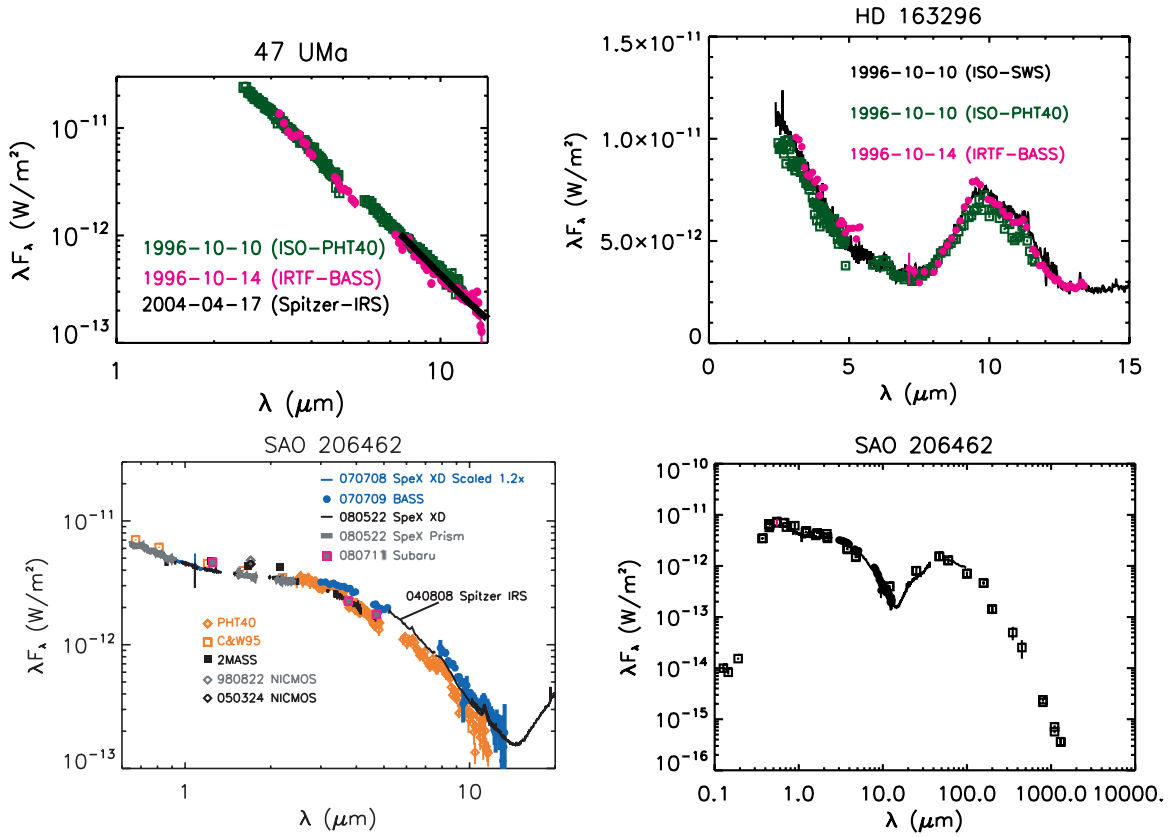

Figure 6. (a) Agreement in near- to mid-IR photometry and spectrophotometry for noncontemporaneous observations of an exoplanet host star, 47 UMa: ISO PHT40 spectrophotometry, IRTF/BASS spectrophotometry, and *Spitzer* IRS data agree to within 10%. (b) A similar level of agreement is seen for contemporaneous ISO SWS, PHT40 and BASS data for the Herbig Ae protoplanetary disk system HD 163296. (c) The near and mid-IR SED of SAO 206462, obtained using observations from 1992 to the present. All dates are given in UT, and are listed in Tables 3 and 4. Significant variability is detected from 1 to 10 μm, consisting of changes in flux and shape of the SED, in marked contrast to Herbig Ae protoplanetary disks such as HD 163296 or MWC 480 (Sitko et al. 2008). The NIR and mid-IR photometry of Coulson and Walther shows good agreement with the ISO PHT-40 spectrophotometry, and represent the SED at the point that the flux at *J* is highest (high-*J* state, gold symbols). The BASS, Spex 070708 data and the *Spitzer* IRS data correspond to epochs where the NIR excess is smaller at *J*, but larger at *L* and *M* (low-*J* state, blue symbols). (d) The full SED using a limited set of the near-IR data.

M′ bands (Leggett et al. 2003), using the flux calibration of Tokunaga & Vacca (2005).

2.6.5. MIPS SED

A low-resolution ($R \sim 1525$), 5498 μm spectrum of SAO 206462 was obtained on 2005 February 27 by the *Spitzer Space Telescope* (*Spitzer*; Werner et al. 2004) using the Multiband Imaging Photometer for *Spitzer* (MIPS; Rieke et al. 2004) in its SED observing mode. Lu et al. (2008) describe the operation and calibration of the SED mode. For SAO 206462, the SED mode observations were made using an AOR requesting six cycles of 3 s exposure per frame. The achieved total on-source integration time of 113.2 s.

Data reduction was accomplished using the data analysis tool (DAT) developed by the MIPS instrument team (Gordon et al. 2005). The background was removed by individually subtracting each sky exposure from the preceding exposure having SAO 206462 centered in the slit. Specific reduction and calibration relevant to SED-mode observations, which include illumination and slit-loss corrections, the dispersion solution, and flux calibration, are discussed in detail by Lu et al. (2008). We used the default 5 pixel-wide extraction aperture to construct the one-dimensional, wavelength and flux-calibrated spectrum of SAO 206462. This spectrum has previously been discussed in Brown et al. (2007).

2.7. The SED of SAO 206462

The assembly of the IR SED of SAO 206462 is discussed in Appendix A, with the 0.6–10 μm data shown in Figure 6(c). The amplitude and shape of the SED varies significantly over 1–10 μm. The full SED with selected NIR data is shown in Figure 6(d). After assembly, the full SED of SAO 206462 has a distinctive two-component shape with local maxima at 2.5 μm and 50–60 μm, similar to other Herbig stars with Meeus et al. (2001) group I classifications or the more recently identified "gapped" or "cold" disks (Brown et al. 2007; Figure 6(d)). Closer examination of the cool dust component shows additional structure in the 13–90 μm range: the sharp rise longward of 13 μm, noted by Brown et al. (2007), a local maximum near 20 μm, a local minimum near 30 μm, and what appears to be a somewhat convex SED from 50 to 90 μm.

As noted in Appendix A, SAO 206462 exhibits significant warm dust variability in both amplitude and in temperature, which has not been previously reported for this star. Jet-driving Herbig Ae stars such as HD 163296 and MWC 480 exhibit correlated changes at 3.7 and 10 μm, with the largest amplitude variations seen at 3.7 μm (HD 163296; 42% amplitude at 3.7 μm, with 16% amplitude at 10 μm; MWC 480; 50% amplitude at 3.7 μm and 24% at 10 μm; Sitko et al. 2008). The variability also differs from UXORs such as SV Cep which show large amplitude variation in the optical, and in the

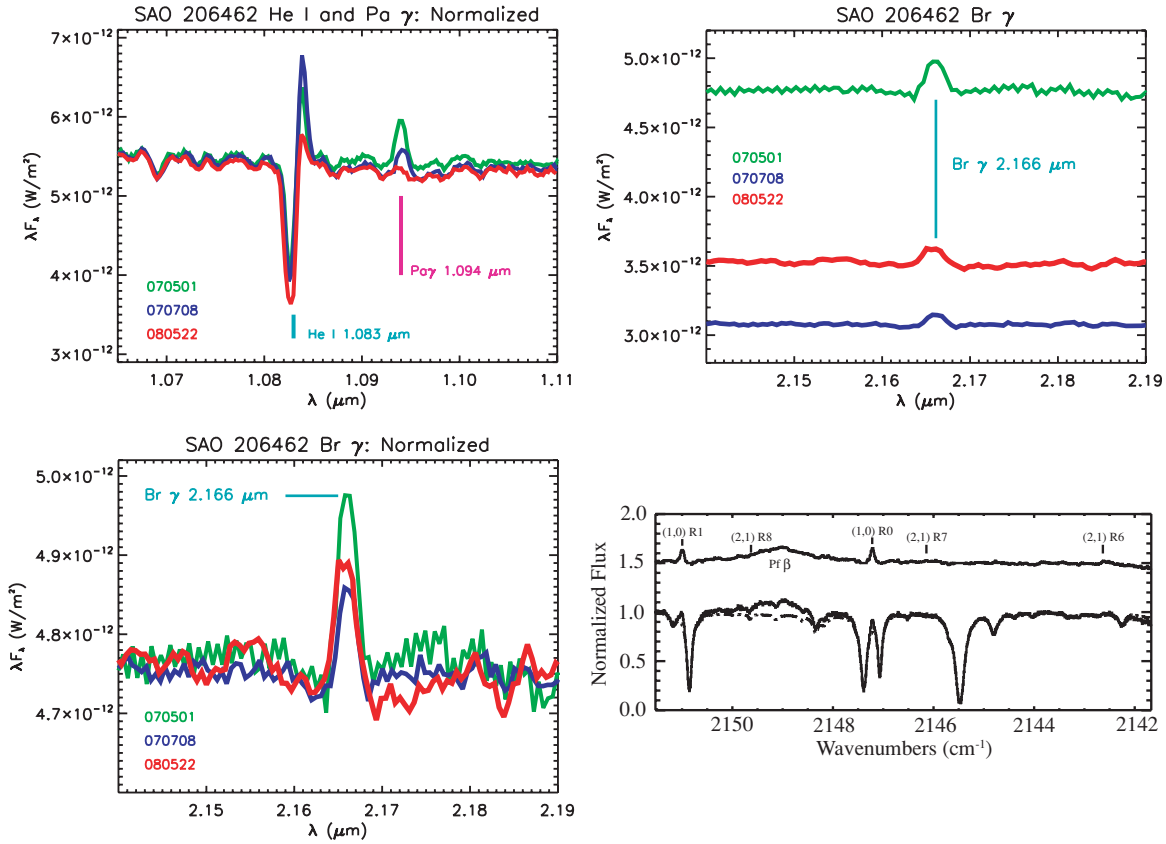

Figure 7. IR emission lines of SAO 206462. (a) Continuum-normalized He I 1.083 μm and H I Pa γ profiles. He I shows a type I P Cygni profile similar to that seen in TW Hya (Dupree et al. 2005), with the strength of the emission uncorrelated with the continuum light. (b) H I Br γ. The strongest emission is associated with the highest continuum level in the SpeX data. (c) Continuum- normalized Brγ emission: the equivalent width of the Brγ emission changes more steeply than the simple linear correlation expected if the NIR continuum measures the accretion rate. (d) Phoenix mid-IR spectrum showing CO transitions and H I Pfβ. The lower spectral trace shows the telluric standard HR 5671 together with the inferred continuum below the H I profile. The upper trace shows the continuum normalized spectrum.

far-IR, with modest variability at 3.5 and 12 μm (SV Cep, 60% amplitude in optical, 100% at 100 μm, reduced amplitude at 3.5 and 12 μm; Juhász et al. 2007). To date, significant variation has been seen in SAO 206462 on timescales as short as six weeks. Variability is not limited to the continuum, but includes several NIR emission lines (Figure 7(a)–(c)), including Brγ.

2.8. High-Resolution Gemini South/Phoenix Spectrum

SAO 206462 was observed on 2008 March 23 using the Phoenix echelle spectrograph (Hinkle et al. 1998, 2000, 2003) on Gemini South as part of program GS-2007A-C-3. Phoenix provides a resolution of 50,000 and a spectral grasp of $\sim$10 cm^{-1} at 5 μm. The spectrum was obtained with a $0\farcs34\times14''$ slit, which was placed in the default east–west orientation, resulting in 6 km s^{-1} resolution in the dispersion direction. Subexposures were obtained with a $5''$ nodding throw in an A-B-B-A nod pattern. The M2150 filter was used, centered on 2147 cm^{-1}. A total of 16 minutes of integrated data were obtained for SAO 206462. The data were observed and reduced as described in Brittain et al. (2003) and Brittain et al. (2007, 2009), using a $0\farcs9$ extraction slit (11 pixels wide). Telluric absorption lines were corrected by dividing the spectrum with a telluric standard (HR 7121) observed at the same air mass. Areas with transmittance less than 60% were omitted. The $v = 1$–0 ^{12}CO emission and broad H I Pf β emission are shown in Figure 7(d). No emission is detected from $v = 2$–1 ^{12}CO.

3. RESULTS

In this section, we first discuss the results derived from the coronagraphic imagery, and then turn to the FUV data, followed by gas in the inner disk.

3.1. The Scattered Light Disk

The combined PSF-subtracted images of SAO 206462's disk at F110W and F160W are shown in Figure 2, and the azimuthally medianed radial SB data are shown in Figure 8. At F110W, excess light can be traced from $0\farcs42$ to $1\farcs05$, with S/N $\geqslant$ 3.2 in all radial zones from $0\farcs42 \leqslant r \leqslant 0\farcs92$ and a peak SB of 18 $\pm$ 1.6 mJy arcsec^{-2} at $0\farcs42$ (Figure 8(a)). The flux density from $0\farcs42$ to $1\farcs0$ is 9.7 mJy $\pm$ 7%, corresponding to a scattering fraction of 0.45% relative to the star at 1.1 μm. When compared with representative PSF–PSF difference imagery, the excess light is a 14σ detection. By $r = 0\farcs93$, the azimuthally medianed disk radial SB has dropped to 0.1 mJy arcsec^{-2}, indicating an unusually steep radial profile. From $0\farcs42 \leqslant r \leqslant 0\farcs93$, the F110W radial SB data cannot be fit with a single power law (Figure 8(b)). A good fit is achieved for $0\farcs60 \leqslant r \leqslant 0\farcs93$, with SB$\propto r^{-9.6}$. At $r \leqslant 0\farcs60$, the SB rolls over.

At F160W, the disk is detected over a more limited range, primarily due to the imperfect star-PSF template color match, but reaches 30 mJy arcsec^{-2} at $0\farcs46$. The azimuthally medianed radial SB profile is similar to the F110W data from $0\farcs6$ to $0\farcs75$, but lacks the roll-over interior to $0\farcs60$ (Figure 8(c)). The F160W/F110W radial SB ratio of the disk (Figure 8(d))

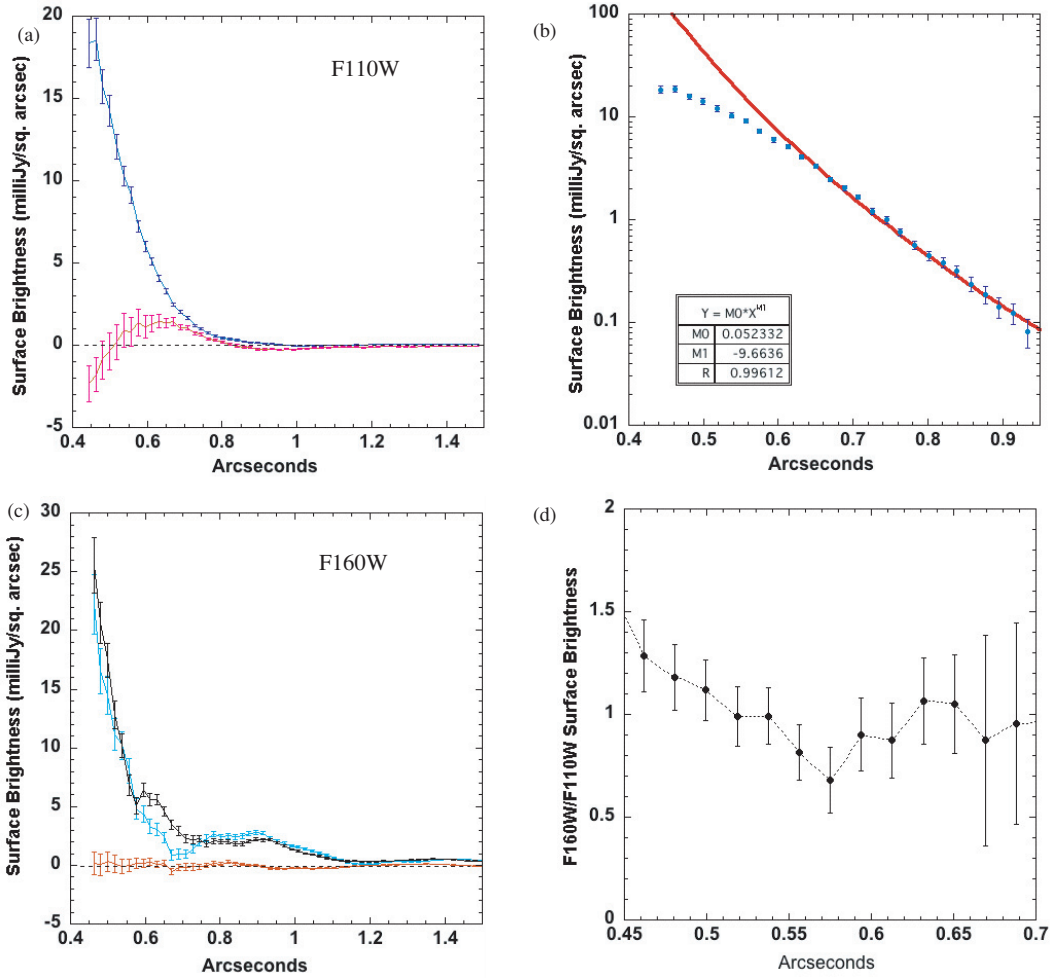

Figure 8. Disk azimuthally medianed SB: (a) F110W, from the first visit, and residuals from a PSF–PSF subtraction handled similarly to the SAO 206462 data. The disk is a 14σ detection near the coronagraph's inner working angle. (b) Power-law fit. (c) SB forF160W. PSF subtraction results for the single science target orientation are shown with each PSF template, together with a red PSF–PSF pair. (d) The F160W/F110W radial SB ratio of the disk. While a shallow color gradient is seen for $r \lesssim 0\farcs59$, overall the disk is significantly blue compared to the star ($f*_{F160W}/f*_{F110W} = 2.27 \pm 0.60$). Error bars in panels a–c are the standard deviations of SB measures (and ratios in panel (d) from all unmasked pixels in concentric 1 pixel (75.8 mas) wide annuli (radially incremented in 1/4 pixel-wide steps) about the corresponding annular medians. The 1σ measurement errors do not include a systematic $\lesssim$20% uncertainty in the absolute calibration of the SB due to the uncertainties in the flux-density renormalization (brightness scaling) of the PSF templates before image subtraction.

exhibits a shallow decline from a peak value of $\sim$ 1.25 at $r = 0\farcs46$ to $\sim 0\farcs57$, but is near unity from $0\farcs59$ to $0\farcs70$. The star itself is red in [F110W] − [F160W]. By fitting TinyTim model PSFs to our unocculted F110W images of the star,[22] obtained contemporaneously with our 2005 epoch coronagraphic disk images, we find the epochal [F110W] magnitude of the star to be 7.48 ± 0.03. No contemporaneous F160W stellar images were obtained along with the 1998 epoch disk observations by Augereau et al. (2001). Hence we adopt the 2MASS catalog *H*-band for SAO 206462 of 6.59 ± 0.03 as a very close proxy to the NICMOS F160W band. As indicated in Table A1, SAO 206462 has been seen to be photometrically variable by $\sim$ 23% peak-to-peak at $\sim$ 1.7 μm. We adopt this as a representative *systematic* uncertainty in the 1998 epoch F160W magnitude. From these stellar magnitude estimates we find the [F110W] − [F160W] color index of the star to be +0.89 ± 0.23. Hence, on the azimuthal median, the disk grains (with F110W/F160W SB ratio $\sim$ unity; i.e., [F110W] − [F160W] $\sim$ 0) are significantly bluer at all radii sampled by NICMOS than would be expected for spectrally neutral scattered starlight (stellar F160W/F110W flux density ratio = 2.27 ± 0.60). The intrinsic [F110W] − [F160W] colors of the outer disk are consistent with scattering either by a surface layer of small grains or with a water-ice and silicate mixture. Additional wavelength coverage is required to better establish the full reflectance spectrum of SAO 206462's disk. The scattered light disk as seen by NICMOS and STIS is smaller than the angular extent of the disk inferred from 20 μm imaging (Doucet et al. 2006), but is in excellent agreement with the disk imaged in the submillimeter (Pontoppidan et al. 2008).

3.2. Inclination Constraints for SAO 206462

As noted in the introduction, a wide range of inclination estimates or measurements are in the literature for SAO 206462. NICMOS coronagraphic imagery provide inclination constraints for the outer, dust disk only. We assess the inclination of the SAO 206462 light-scattering disk simply assuming an

[22] Because of its brightness our F110W SAO 20642 stellar images saturated in their PSF cores (inside the first Airy minimum), aperture photometry is problematic. Thus we use TinyTim, an optical modeling tool that replicates *HST* PSF with very high fidelity (available from STScI at http://www.stsci.edu/software/tinytim/tinytim.html), to fit the deeply exposed broad wings of the stellar PSF with χ-square minimization in subtraction residuals to ascertain the stellar brightness.

intrinsically circularly (azimuthally) symmetric disk if viewed face-on, but actually seen in sky-plane projection. To quantitatively estimate the line-of-sight inclination angle (viewing geometry), we use the NICMOS F110W image alone given the higher spatial resolution and superior coronagraphic starlight rejection than in the F160W band. Following Schneider et al. (2009), we fit five, presumed elliptical, SB isophotes (from 2 to 10 mJy arcsec^{-2}, equally spaced in brightness) to the two-roll combined, PSF-subtracted disk image. In doing so we excluded data from 270° < P.A. < 360° due to image data quality issues in that azimuthal sector of the disk (see Section 2.1.1). Averaging the five fitting solutions, we find a best-fit (minor:major) axial ratio of 0:934 ± 0.009, corresponding to an inclination angle of 20.°8 ± 1.°5 from face on, with a celestial position angle for the major axis of 55° ± 5° east of celestial north, in good agreement with the disk major axis derived by Pontoppidan et al. (2008) from the circumstellar gas. The fitting solutions for the F160W data are not as robust, but are consistent with an inclination of $\lesssim$ 20° from face-on, so we conservatively adopt an $i = 20°$ as an upper limit based on both the NICMOS F110W and F160W images.

Separately, we note that the PSF subtraction residuals in the roll-differenced imagery (Figure 1(b)) are azimuthally symmetric within a sensitivity-limited $r \leqslant 3''$ of SAO 206462. Symmetric roll-difference residuals occur either when there is no circumstellar nebulosity beyond the radius of the coronagraphic spot, or when the nebulosity is symmetric about the star. The firm detection of a scattered-light disk at both 1.1 and 1.6 μm (Figure 2(a) and (b)) using a suite of PSF template stars, firmly excludes the first possibility. The azimuthal symmetry of the PSF subtraction residuals in this region of the roll-subtracted image, where the disk is robustly detected with PSF template subtraction, is consistent with a close to face-on viewing geometry as was derived from isophote fitting of the PSF template subtracted image. In particular, A disk extending to 1.″5 and viewed at $i = 45°$, as reported by Doucet et al. (2006), or an outer disk inclination at the 60° noted by Fedele et al. (2008) would produce distinctive positive/negative disk images in the roll-differenced imagery, and is not seen. A disk inclined by 45°–60° would also have been expected to produce detectable H_2 absorption in *FUSE* FUV spectra, such as is seen in the spectrum of HD 163296 (Deleuil et al. 2005) or MWC 480 (Martin-Zaïdi et al. 2008), in marked disagreement with the nondetection for SAO 206462 as reported by Martin-Zaïdi et al. (2008). Our inclination upper limit of 20° is consistent with Dent et al. (2005): we adopt their $i = 11° \pm 2°$ for the rest of this paper.

3.3. Limits on Wide Companions

The closest point source to SAO 206462 as seen in the STIS coronagraphic imagery (Figure 3) lies 4.″1 from SAO 206462, and is typical of several tens of sources in the STIS field of view. Augereau et al. (2001) had noted a 5.″8 binary SE of SAO 206462 as a potential companion to SAO 206462. AO 206462s proper motion is (−20.60 ± 2.60, −25.70 ± 2.20) mas yr^{-1} in R.A. and decl. (Hog et al. 1998), or 178 ± 18 mas over the 5.41 yr between the two NICMOS observational epochs. Differential astrometric measures of the position of the binary with respect to SAO 206462 revealed a displacement in its position of ≈ 150 mas opposite the direction of SAO 206462s proper motion. We conclude, therefore that the binary is a background object, and is not physically associated with SAO 206462, consistent with its nondetection in the FUV (Figure 3(b)). The absence of comoving objects beyond the disk of SAO 206462, as demonstrated by the NICMOS imagery and the ACS F122M data suggests that SAO 206462 is an isolated, single star.

3.4. Limits on Close Companions

We used the F110W coronagraphic images at both field orientations to search for faint stellar or substellar companions to SAO 206462 both within, and in close proximity to, the outer regions of the scattered light disk. Because the disk is close to face-on, subtracting the SAO 206462 image at the second field orientation from the first image greatly reduces the light from the disk as well as residual starlight from the underlying stellar PSF which is unsuppressed by the coronagraph (Lowrance et al. 1999). In such a "roll-difference" (or active astrometric differential imaging) image any point-like companion candidates appear as a positive and negative pair separated by the differential roll angle along an arc centered on the star. No companions were found (Figures 1 and 2). To assess our companion detection sensitivity limits, we implanted noiseless, model "PSF stars" in rings of varying angular radii (positive images flanked by two negative images) about the position of SAO 206462 in the difference image. We adjusted the flux density scaling of the implants until robust detections of positive/negative image pairs were obtained. The 5σ (above the standard deviation measured about the median background in 3 × 3 pixel regions along a corresponding annulus in the difference image before implantation) detection limits were found to be: ΔF110W = 5.89 (± 0.27) + 6.11*r(arcsec). These limits are valid at all circumstellar azimuth angles, except in a sector ≈ 60° in arc-length at $r < 0.''6$ where a localized 2-roll PSF-subtraction artifact raises the companion detection limit by approximately +1.0 F110W (mag). To explore closer to the star, we have also used the core-saturated direct images to search for companions interior to 0.″5. The detection sensitivity, similarly determined using model implantation, but with template PSF subtraction rather than 2-roll image subtractions results in companion detection sensitivities of ΔF110W ranging from +3.0 ($r = 0.''2$) to +4.5 at $r = 0.''4$. Both detection limits are shown in Figure 9. At the inner working angle of the coronagraph, the F110W coronagraphic 5σ detection limit corresponds to a spectral type of M6V (Leggett et al. 2002).

The STIS coronagraphy indicates the presence of a red PSF component ($\lambda_{\rm eff} \geqslant 8000$ Å) accounting for 3.4% of the light from SAO 206462, and no second set of diffraction spikes, such as are conspicuous from $K-G$ companions (Grady et al. 2004). This suggests that any red component either lies within 0.″05 of the Herbig Fe star, or that the star itself is redder than expected for an F4V star. Spectroastrometry of SAO 206462 (Baines et al. 2006) excludes a stellar companion exterior to 0.42 AU. We conclude that there are no close *stellar* companions to SAO 206462, but cannot exclude the presence of brown dwarf or planetary mass bodies within the disk.

3.5. The Source of the Red Optical Color for SAO 206462

In principal, the red color of SAO 206462 could be due to the presence of a previously unrecognized, extremely close, stellar companion, selective extinction, or is intrinsic to the star.

Selective Extinction. HD 135344A lies 20.″8 (2900 AU) to the NNE of SAO 206462 and has a proper motion vector (−17.9, −31.0; Roesser & Bastian 1988) which agrees with that of SAO 206462 to within 1σ. With a spectral type of A0V,

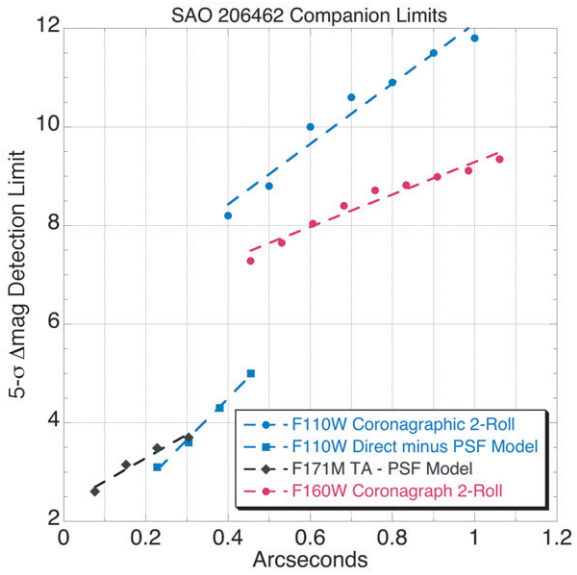

Figure 9. 5σ detection limits for faint companions to SAO 206462 within the circumstellar disk. Roll-difference detection limits for the coronagraphic imagery are shown in blue, with direct imagery minus a PSF model shown in red and the shallow medium band F171M minus PSF model shown in black.

$E(B-V) = 0.071$, HD 135344A is 1.76 mag fainter than HR 4796A (A0V, $d = 67 \pm 3$ pc; Jura et al. 1998) after correction for extinction at V. The magnitude difference corresponds to a distance for HD 135344A of $\sim$163 $\pm$ 3.8 pc, in reasonable agreement with this star being a member of the same association as SAO 206462. van Boekel et al. (2005) identify SAO 206462 as a member of Sco OB2-3 at $d = 140$ pc, in agreement with our estimate for the distance to HD 135344A. SAO 206462 has $B-V = 0.498$. Dunkin et al. (1997a, 1997b) find F4V for this star, although Guimarães et al. (2006) find F8V. At F4V, $B-V = 0.42$, while at F8V $B-V = 0.53$, which is redder than observed for SAO 206462. Adopting F4V for SAO 206462, we find $E(B-V) = 0.078$, in agreement with the extinction toward HD 135344A. Given $i = 11^\circ \pm 2^\circ$, the extinction is likely foreground to *both* stars, excluding the presence of a residual envelope associated with SAO 206462 alone, and is possibly associated with the denser interstellar material bounding the Local Bubble (Lallement et al. 2003). While low, the selective extinction toward SAO 206462 is sufficient to attenuate FUV fluxes by a factor of 2.2 near 1160 Å assuming the extinction law of Sasseen et al. (2002). However, $E(B-V) = 0.078$ is too small to cause significant color-mismatches in the STIS coronagraphic data reduction (Grady et al. 2005) indicating that SAO 206462 must be intrinsically redder than typical of single, slowly rotating mid-F stars.

Stellar Rotation. While the measured $v \sin i$ for SAO 206462 (Dunkin et al. 1997a, 1997b) suggests a slowly rotating, intermediate-mass star, by combining the $v \sin i$ data with the disk inclination, we find that $v_{\rm eq} = 360^{+80}_{-55}$ km s^{-1}, making SAO 206462 an extremely rapid rotator for a mid-F star. This equatorial velocity is higher than seen in either Altair or Vega. The star, therefore, should exhibit gravity darkening effects at least as large, or a latitudinal temperature gradient $\geqslant$2000 K, as observed for those systems (Aufdenberg et al. 2006; Peterson et al. 2006a, 2006b) or for Achenar (Domiciano de Souza et al. 2003; Carciofi et al. 2008). With this large a temperature gradient, the equatorial belt of the star is cooler than the Sun, making the habitable zone in this system similar to that of the Solar System. Moreover, the star should appear redder than expected based on spectral type diagnostics near 4200 Å, given the wide bandpass of the STIS coronagraphic imagery. One immediate implication of the presence of a large temperature gradient is that no single-temperature stellar model would be expected to fit the photospheric spectrum, but following Grady et al. (2007), a linear combination of single temperature models may provide a reasonable approximation.

3.6. Accretion and Mass Loss in SAO 206462

The FUV emission lines in the spectrum of SAO 206462 are present both in the spectra of actively accreting Herbig Ae stars and in FUV spectra of active, late-type stars. Accreting and jet-driving Herbig Ae stars have broad O VI (1032, 1038 Å) profiles (FWHM $\sim$ 2.2 Å) which do not correlate with the stellar $v \sin i$, and also have distinctive, double-peaked C III λ1176 profiles (Grady et al. 2004 for HD 104237). In contrast, active, late-type stars have emission profiles which correlate with the stellar $v \sin i$, with blocky emission profiles at low $v \sin i$, and cuspy profiles at high $v \sin i$ (Simon et al. 2002). The HWHM of the C III 977 Å profile is 1.1 Å, a factor of 5.5 times broader than typical of young nonaccreting F3–F7 stars, and is too broad to be produced by stellar activity alone in a low $v \sin i$ star. The large profile width is similar to that observed in TW Hya and actively accreting Herbig Ae stars. At O VI, the 1032 Å line has FWHM $\approx$ 1 Å, again broader than nonaccreting F stars observed by *FUSE*, but narrower than accreting Herbig Ae stars such as MWC 480 (Figure 5), or HD 104237 (Grady et al. 2004). At C III λ1176, the profile is stronger than seen in the accreting Herbig Ae stars, lacks the double-peaked profile of the jet-driving systems, and has a blocky emission profile in that feature, more closely resembling moderate $v \sin i$ late-type stars (Redfield et al. 2002).

The presence of strong wind absorption is characteristic of Herbig Ae star spectra. P Cygni profiles characterized by emission longward of line center and absorption shortward of line center are commonly observed in the UV and FUV toward Herbig Ae stars with low-inclination disks such as AB Aur (Roberge et al. 2001), and in near-IR lines such as He I 1.083 μm (Figure 7(a); Kwan et al. 2007). Dupree et al. (2005) have also reported similar asymmetry in *FUSE* spectra of the classical T Tauri star TW Hya which is viewed at 7° inclination (Qi et al. 2004). Just as for TW Hya, the C III 977 Å profile for SAO 206462 is highly asymmetric (Figure 4) with the bulk of the emission longward of 977 Å, and extending to at least +400 km s^{-1}. Either by mirroring the observed C III profile, or in comparison to the A7Ve Herbig Ae star HD 139614, the flux deficits shortward of 977 Å indicate absorption to at least -300 km s^{-1}. Absorption associated with O I λ976.448 and with O I$^*\lambda\lambda$977.958, 978.617 is also present, and displaced shortward of the rest wavelengths. For these transitions we infer terminal velocities near -120 km s^{-1}. The absence of C II $\lambda\lambda$1036.336, 1037.017 emission shortward of the 1037.017 feature suggests that these lines are also affected by wind absorption, with a terminal velocity of at least -200 km s^{-1}. A progression of terminal velocity from -120 km s^{-1} in neutral, atomic gas, to -200 km s^{-1} in singly ionized gas, and then -300 km s^{-1} in moderately ionized gas is indicative of the presence of an accelerating wind or jet from SAO 206462.

Pontoppidan et al. (2008) identify P.A. = 56° $\pm$ 2° for the celestial orientation of the disk major axis, in agreement with our NICMOS F110W data, which would place the minor axis along P.A. = 146° $\pm$ 2°. PMS stellar jets typically project along the system minor axis. Despite the presence of the wind features,

no Herbig–Haro knots, as are commonly seen in association with jets (Grady et al. 2000, 2004; Devine et al. 2000), are detected in either the STIS coronagraphic imagery or the ACS FUV imagery.

Our SpeX data show type I P Cygni emission in He I 1.083 μm, with weakly variable absorption, relative to the continuum, and highly variable emission. The He I emission does not appear to be correlated with the continuum. Our high state Brγ from 2007 May 1 has an equivalent width of 1.58 Å, slightly above the Garcia Lopez et al. (2006) measurement, while the low state on 2007 July 8 has an equivalent width of 0.82 Å is approximately a factor of 2 below the high state. Following Garcia Lopez et al. (2006), the Brγ therefore indicate that the accretion rate is variable by a factor of ~ 2, assuming no continuum variability. However, while the Brγ and Paγ emission are strongest in the highest flux spectrum in our sample, the strength of the emission does not show a simple correlation with continuum flux, as would be expected if both the NIR continuum and the emission are measuring the accretion rate.

Dupree et al. (2005) used the emission asymmetries in TW Hya in C III and O VI to infer the presence of a hot ($T \sim$ 300,000 K), fast ($v_\infty \sim -400$ km s^{-1}) wind. The lack of asymmetry in O VI in SAO 206462 instead suggests the presence of a warm ($T \sim 8000$ K), fast ($v_\infty - 400$ km s^{-1}) wind. Warm winds have been proposed by Simon et al. (2002) as the cause of weak coronal emission in early F Main Sequence stars, while supersonic jets are associated with the accreting Herbig Ae stars HD 163296 (Devine et al. 2000), HD 104237 (Grady et al. 2004), and MWC 480 (B. Stecklum et al. 2009, in preparation). The STIS and ACS data provide no indication that SAO 206462 drives a jet. The strength of the C III 977 Å absorption, together with the presence of O I and C II wind absorption, suggests a mass-loss rate intermediate between TW Hya ($\dot{M} \approx 10^{-11}\ M_\odot$ yr^{-1}; Dupree et al. 2005) and HD 163296 ($\dot{M} \approx 10^{-8}\ M_\odot$ yr^{-1}; Wassell et al. 2006).

3.7. Detection of FUV Excess Light

When scaled to the V magnitude of SAO 206462, photospheric spectra for mid-F stars, have flux densities near 10^{-17} erg cm^{-2} s^{-1} Å^{-1}, a factor of 100 below the *FUSE* faint limit. In contrast to mid-F stars from Tuc-Hor, which show only a sparse emission-line spectrum typical of saturated chromospheric and transition region activity, SAO 206462 has a weak continuum marginally detected down to 1020 Å (Figure 4). After correcting for $E(B-V) = 0.078$ using the FUV extinction law of Sasseen et al. (2002), we find a continuum flux of 1.3×10^{-14} erg cm^{-2} s^{-1} Å^{-1} near 1160 Å. This is a factor of 3.5 fainter than the continuum seen in the lightly reddened star HD 104237 as seen by *FUSE*. We conclude, therefore that we have detected the FUV excess light associated with the accretion luminosity of SAO 206462, and adopt the Garcia Lopez value for the accretion rate of $5 \times 10^{-9}\ M_\odot$ yr^{-1}. This accretion rate corresponds to a Brγ equivalent width toward the high end of the range seen in our SpeX observations, and is similar to the accretion rate estimated by B. Stecklum et al. (2009, in preparation) for MWC 480. If we assume that mid-A stars, such as MWC 480, lack strong chromospheric emission and that the emission seen in MWC 480 is typical of its accretion rate, at $d = 140$ pc, only 10% of the C III λ1176 emission in SAO 206462 can be due to accretion. At O VI, any accretion-related emission can account for at most 1/3 of the observed flux. Thus, while accretion contributes to the profiles, stellar activity dominates the FUV line emission.

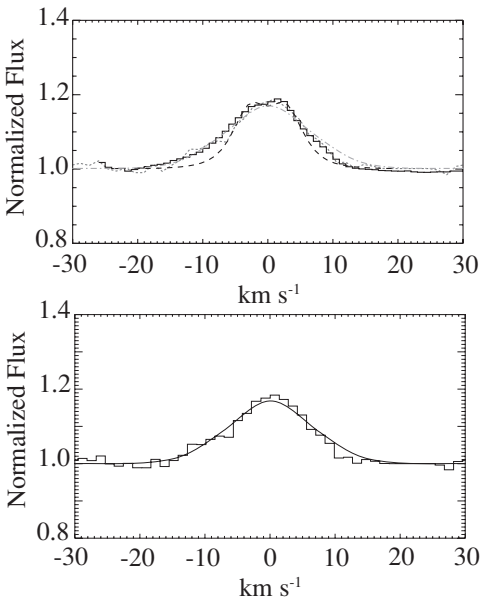

Figure 10. ^{12}CO profiles. Upper panel: CRIRES data from Pontoppidan et al. (2008) are shown together with their model (dashed, black line), the 2008 average PHOENIX data (gray, dotted line), and the excitation model (gray dot-dashed line). Lower panel shows the PHOENIX data (histogram) with the excitation model as a solid line.

3.8. Molecular Gas in the Inner Disk

Warm molecular gas is commonly observed in the inner disks of accreting T Tauri (Najita et al. 2003) and Herbig Ae/Be disks (Brittain et al. 2007), and can be either thermally excited or UV fluoresced. Such emission is present in our mid-IR Phoenix spectrum (Figure 7(d)). Average ^{12}CO emission line profiles for SAO 206462 are shown both for the data from Pontoppidan et al. (2008) from 2007 and for our 2008 observation in Figure 10. The nondetection of the $v = 2$–1 ^{12}CO emission lines together with the detection of the $v = 1$–0 RO and R1 lines indicates that the molecular gas in the inner disk of SAO 206462 is not UV fluoresced, in marked contrast to the B9.5Ve transitional disk system HD 141569A (Brittain et al. 2007). The average emission line profiles, normalized to their respective continua, agree to within 1%. We confirm the profile asymmetry shown by Pontoppidan et al. (2008). The lack of significant profile variability for the CO emission (Figure 10), in the presence of striking variations for the atomic emission lines (Figure 7) and in the presence of the NIR continuum variability suggests that the molecular gas is associated with the warm dust, rather than the near-stellar gas. The HWZI of the CO line profile is 18 ± 2 km s^{-1}, and is consistent with molecular gas extending into $r = 0.27^{+0.07}_{-0.05}$ AU. We have modeled the emission profile using the disk model described in more detail in Brittain et al. (2009), adopting a stellar mass of 1.7 $M_\odot$, a turbulent width of 1.5 km s^{-1}, and a disk inclination of 14°, following Pontoppidan et al. (2008). We set the inner radius of the molecular gas at 0.3 AU and $T(r) = 10^3\ (r/1\ \mathrm{AU})^{-0.125}$, with negligible UV fluorescence. The molecular gas temperature is ≈ 1000 K, and the density is 10^{12} cm^{-3}.

4. THE DISK OF SAO 206462

In this section, we consider the distance to SAO 206462, the observational constraints on the disk, then model the SED using these constraints, and discuss the implications for the

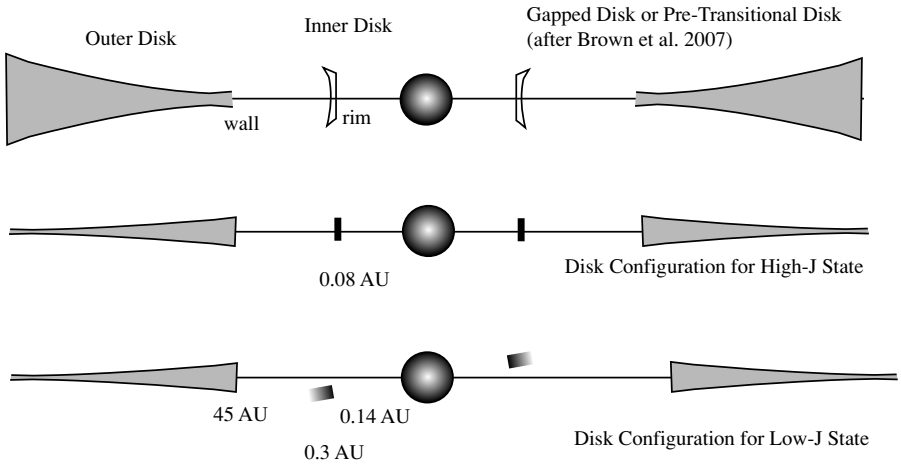

Figure 11. Schematic cartoon for the SAO 206462 system, beginning with the configuration proposed by Brown et al. (2007). Our NICMOS data indicate that the outer disk is not flaring, as shown in the lower 2 panels, but indicate that the warm dust component has a variable inner radius. At its maximum extent, the inner disk can be fit with a disk model inclined by 10° with respect to the outer disk, in partial confirmation of the interferometric results of Fedele et al. (2008). In the lower panel, the outer disk is asymmetric, consistent with the eccentric cavity imaged by Pontoppidan et al. (2008).

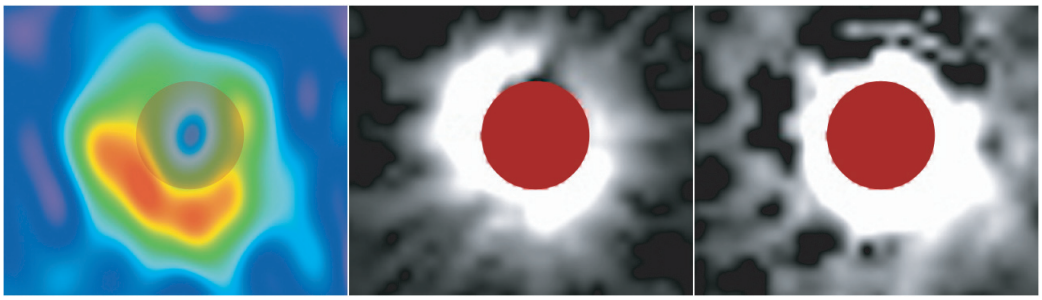

Figure 12. Comparison of the 850 μm continuum imagery of SAO 206462 (Pontoppidan et al. 2008) with the NICMOS 1.1 and 1.6 μm coronagraphic imagery. All three images are shown with north up and east to the left. The $r = 0\farcs3$ region occulted in the NICMOS data are shown as a shaded circle against the SMA data and as filled circles in the NICMOS imagery. The cavity, which is eccentric, is entirely occulted in the NICMOS data. Some of the features seen in the submillimeter for the outer disk may be present in the 1.1 μm data (at celestial position angles $0° <$ P.A. $< 270°$ where the NICMOS data are valid, see Section 2.1.1), but are less clear in the 1.6 μm imagery.

interpretation of the disk. A cartoon of the system, based on Brown et al. (2007) is shown in Figure 11, while the submillimeter and NIR imagery are shown side-by-side in Figure 12 for comparison. Both sets of imagery place the outer edge of the disk slightly beyond $1''$: the mapping to AU, as well as the location of the outer edge of the submillimeter cavity which we term the "wall" to distinguish it from the inner edge of the warm dust (the "rim"), depends upon the distance to the star.

4.1. The Distance to SAO 206462

Two distances to SAO 206462 have been used in the literature. The first, $d = 84$ pc, is based on the assumption that SAO 206462 is a Vega analog, e.g., a Main Sequence F star, originally due to Coulson & Walther (1995). The second is based on the identification of the star as being a member of Sco OB2-3 at $d = 140$ pc (van Boekel et al. 2005). Brown et al. (2007) find that the wall lies at 45 AU based on the wavelength of the steep rise in the IR SED. At $d = 84$ pc, this radius corresponds to $0\farcs53$, in the middle of the ring of submillimeter continuum emission and the NICMOS scattered-light disk. At $d = 140$ pc, this radius would be located just interior to $0\farcs3$, in agreement with both sets of imagery.

An alternate argument for the larger distance to SAO 206462 is provided by the FUV data for SAO 206462. The presence of a FUV excess, broad O VI, and a strong stellar wind, as seen in C III are atypical of zero-age main sequence (ZAMS) F stars, such as those in the β Pictoris Moving Group, implying that SAO 206462 must be younger than ~ 12 Myr, and thus not yet on the ZAMS. Adopting $d = 140$ pc, would place the star above the ZAMS, at $t = 8$ Myr. At this age, accretion and mass-loss signatures are known for other, well dated systems such as TW Hya (Dupree et al. 2005).

At $d = 140$ pc, L_X for SAO 206462 is similar to other accreting, Herbig Ae and Fe stars (Skinner et al. 2004; Hamaguchi et al. 2005), and within the observed range for non-accreting ZAMS F stars (de la Reza & Pinzón 2004). CCD-resolution X-ray data, such as will be provided by a planned *Chandra* observation, are needed to establish whether the X-ray spectrum of SAO 206462 is dominated by coronal activity or accretion. However, if we adopt an age of ~ 8 Myr, the model-dependent upper limit to the mass of a companion to SAO 206462 is likely in the range of $\sim$ 50–80 $M_{\rm Jup}$. Brown dwarfs in this mass and age range have typical $L_x \approx (2\text{–}3) \times 10^{27}$ erg s^{-1} (Tsuboi et al. 2003). The *ROSAT* detection is consistent with the X-ray emission arising on the Herbig F star. We therefore adopt $d = 140$ pc for the remainder of our discussion of the disk.

4.2. Modeling the Disk

At $d = 140$ pc, the NICMOS and submillimeter data reveal a disk extending ~ 150 AU from the star, $3\times$ as large as the solar system. For SED fitting purposes, we approximate the star

as a linear combination of Kurucz (1993) 6250 K and 5500 K, $\log(g) = 4.5$, models.

Our upper limit on the outer disk inclination is consistent with an essentially face-on viewing geometry, and is in agreement with both the millimeter CO observations (Dent et al. 2005) and with the inner gaseous disk inclination (van der Plas et al. 2008; Pontoppidan et al. 2008), but in marked disagreement with interferometric data for the warm dust (Fedele et al. 2008). The outer disk has an unexpectedly steep radial SB profile from $0\farcs42 \leqslant r \leqslant 1\farcs05$ (56 to 147 AU), $\propto r^{-9.6}$, with evidence for a roll-over in the power law at 1.1, but not 1.6 μm. Flared disks should have SB$\propto r^{-2}$, while constant opening angle disks are closer to r^{-3}. The NICMOS SB profile is therefore inconsistent with the flared dust disk geometry adopted by Brown et al. (2007) and Fedele et al. (2008) for the outer disk. The outer disk surface is bluer than the star in the NIR, with some indication of a color gradient across the outer disk (see Figure 8(d)).

Use of interstellar medium (ISM)-like grain distributions (Meeus et al. 2001; Dominik et al. 2003) require ad hoc adoption of high disk inclinations to fit the SED at 60 μm, and large outer disk radii to fit the submillimeter and millimeter data, or were principally focused on accounting for data within the range of the *Spitzer* IRS spectrum (Brown et al. 2007). We now know that the disk outer radii and inclinations in these models are incorrect for SAO 206462: a revised modeling effort is therefore in order. Since there are typically families of models which can reproduce the IR SED, but which can be pruned with knowledge of the system inclination, disk outer radius, and the disk SB as a function of radius, following Grady et al. (2007), we have explored model fits to the available data using the most recent version of the Whitney Monte Carlo Radiative Transfer (WMCRT; Whitney et al. 2003a, 2003b; 2004) code.

The WMCRT code explicitly includes both irradiation from the star as well as internal heating from viscous forces in the disk. It uses a standard flared azimuthally symmetric accretion disk where the density structure is given by

$$\rho(r, z) = \rho_0 \left[1 - \sqrt{\frac{R_*}{r}}\right] \left(\frac{R_*}{r}\right)^{\alpha} \exp\left\{-\frac{1}{2}\left[\frac{z}{h}\right]^2\right\},$$

where the scale height h increases with radius r as $h \propto r^{\beta}$. For the case of hydrostatic equilibrium and conservation of radial mass flow, $\alpha + \beta = 1$. As described more completely by Robitaille et al. (2007), the disk scale height at the dust sublimation radius is set to be that for hydrostatic equilibrium, multiplied by a scale factor. This factor can be smaller than 1 if there is gas or other opacity inside the dust destruction radius, decreasing the amount of stellar flux incident on the inner rim; or it can be used to mimic dust settling. Disks where hydrostatic equilibrium is not present can be modeled by relaxing the condition that $\alpha + \beta = 1$.

In addition, the standard release of this code includes an infalling envelope component (described by Robitaille et al. 2007) that is normally used to include material still falling onto the disk in very young protoplanetary disk systems.

4.3. The Outer Disk

In modeling the outer disk we require a model that reproduces both the IR SED and the disk scattered-light SB profile at $i = 11^{\circ} \pm 2^{\circ}$. For transitional or pre-transitional disks, the wall location is typically inferred from the sharp rise in the IR SED. However, the full SED of SAO 206462 has two portions of the spectrum which rise rapidly with increasing wavelength: one from 13 to $\sim$ 25 μm, and one from $\sim$ 25 to 60 μm, which may correspond to the clumpy structure seen at 850 μm (Figure 11). Unfortunately, the current generation of MCRT models assume that the disks are circularly symmetric. Fits with each wall location are shown in Figure 13. In common with Dominik et al. (2003), we find that ISM-like grain distributions produce SEDs which are too bright at 60 μm and too faint in the submillimeter to be consistent with the available data. *The inclination-constrained SED fit therefore indicates that grain growth is global in the disk of SAO 206462.*

We next adopted the Wood et al. (2002) large-grain, dust opacity model used to successfully model HH 30 and GM Aur (Schneider et al. 2003). This grain opacity model assumes cosmic abundances for carbon to silicates and a gas:dust ratio of 100:1. Cosmic abundances appear to be plausible for the outer disk, since it lacks the steep NIR reflectance spectrum slope seen in HR 4796 A (Debes et al. 2008) and the inner disk of HD 100546 (Ardila et al. 2007), and can be fit with more conventional mixtures of silicate and water ice grains. We have also adopted the same inclination, and wall and outer disk radii as for the ISM-like grain model. Geometrically flat or minimally flared disks with such an outer wall structure, where the wall does not itself shadow the outer disk, result in r^{-3} radial SB profiles (e.g., HD 100546, Grady et al. 2001; HD 169142, Grady et al. 2007; HD 97048, Doering et al. 2007; HD 163296, Wisniewski et al. 2008). In the case of SAO 206462, the steep SB profile at $r \geqslant 0\farcs42$ seen by NICMOS, suggests that this wall shadows the *entire* outer disk. To match the SB data, we use a radial density exponent $\alpha = 1.31$, while the density scale height $\beta = 0.31$. This scale height exponent leads to a disk which is convex upward, or "antiflared," allowing for a steep drop-off in SB with radial distance. We achieve a good fit to the SED from 45 to 58 μm into the millimeter. The adoption of an "antiflared" outer disk is contrary to the interpretation of Meeus et al. (2001) group I SEDs as uniformly arising in flared disks, but is entirely consistent with interpretation of SAO 206462 as a transitional or pre-transitional disk (Brown et al. 2007) where significant grain growth and settling would be expected. *One immediate consequence of the NIR scattered-light imagery is that the shape of the IR SED from 5 to 60 μm is not a robust predictor of the radial extent, illumination, or geometry (e.g., flared vs. flat) of the outer disk.*

Is a gas:dust ratio typical of molecular clouds appropriate for an 8 Myr old Herbig star? Dent et al. (2005) and Thi et al. (2001) both note that the disk of SAO 206462, while having detectable ^{12}CO and ^{13}CO emission, has weak emission for either the fractional IR excess, or the inferred disk dust mass. Historically, this has been treated by assuming that the CO is depleted onto grains in the form of ices, but the scattered-light modeling and SED fitting done to date still assume that the bulk of the CO is in the gas phase. In the Whitney MCRT code decrease in the gas:dust ratio can be approximated by increasing the dust opacity/gram of gas, again assuming that the material is well-mixed. We find good fits for gas:dust ratios of 10:1 (1/10 of the molecular cloud value) with similar geometrical implications. At lower gas:dust ratios, the assumption that the gas and dust are well mixed is likely to break down.

4.4. The Warm Dust Component

SAO 206462 is conspicuous both for the large NIR excess compared to other Herbig stars with similar accretion rates (0.24 L_*), and for temporal variation in both the near and mid-IR SED. Unlike actively accreting proto-planetary disks, such as

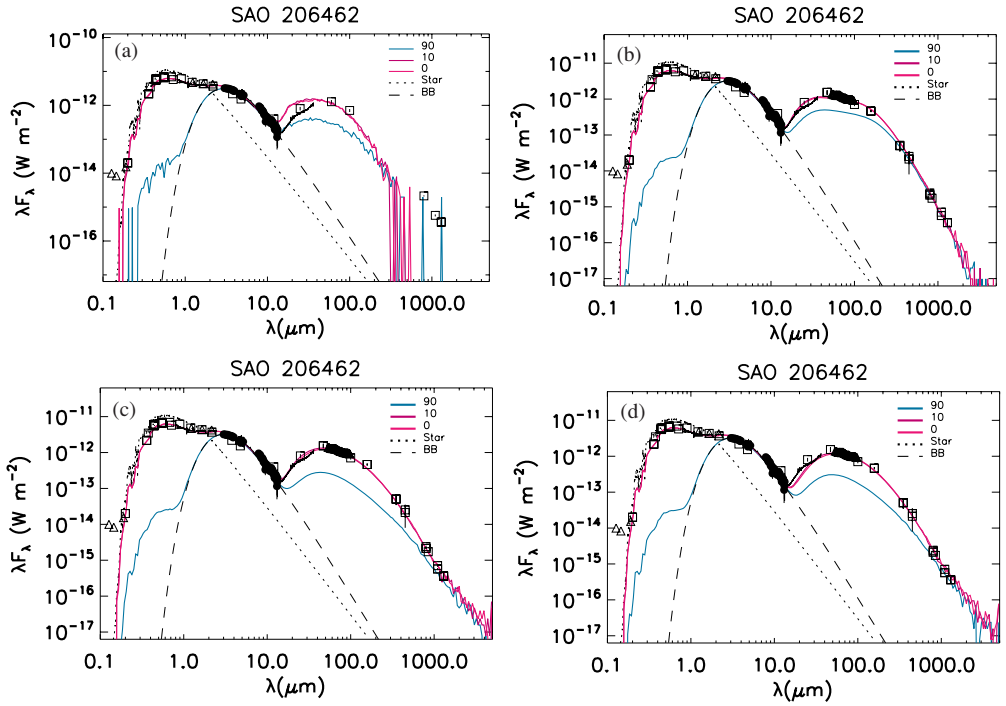

Figure 13. SED fits for two-component disk models with gas to dust ratios of 100:1. Models are shown for 0°, 10°, and 90° inclinations. (a) The inner disk is treated as a single-temperature blackbody. (a) The outer disk is modeled with the Whitney MCRT code, using an ISM-like grain opacity model (Kim et al. 1994), which is dominated by small grains. This model overestimates the 10–50 μm flux while underestimating the submillimeter and millimeter flux. The wall (inner radius of the outer disk) is at $r_{\rm wall} = 45$ AU. Due to the poor fit, this model was terminated with fewer photons than in the other model runs illustrated in this figure, resulting in poor S/N at longer wavelengths. (b) Model fit for the outer disk using the Cotera et al. (2001) opacity model and $r_{\rm wall} = 58$ AU: flux in the 50–90 μm range is underestimated. (c) Model fit using the Wood et al. (2002) grain opacity model successfully used to model HH30 (Cotera et al. 2001) with $r_{\rm wall} = 45$ AU. (d) Same model parameters as for (c), but with $r_{\rm wall} = 58$ AU. SAO 206462 appears to have wall features for the outer disk at two distinct radii, consistent with the clumpy ring and eccentric cavity imaged in the submillimeter (Pontoppidan et al. 2008).

HD 163296 and MWC 480 (Sitko et al. 2008), SAO 206462 does not exhibit correlated near and mid-IR variations with the excess light increasing and decreasing in tandem, or evidence for time-dependent illumination of the outer disk (Wisniewski et al. 2008). We also do not see the anticorrelation with large amplitude optical light variations seen in SV Cep (Juhász et al. 2007), excluding UX Orionis-type variable obscuration of the star as the source of the variability. Instead, the variations are wavelength dependent. Based on the available data, we have identified two extreme states: one where the IR excess is large at *J*, and low at *L* and *M* bands, and vice versa (Figure 6(c)).

High-J state. The current version of the WMCRT code is not normally able to accommodate the presence of a detached inner disk. For the warm dust component in the high-*J* state, unweighted blackbody curves do not fit the data, producing too shallow a drop-off with increasing wavelength. Next, we explored fitting with a blackbody times an emissivity proportional to the wavelength. Generally, emissivities with a steep wavelength dependence (e.g., $\lambda^{-0.8}$) are characteristic of grains which are smaller than the wavelength corresponding to the peak of the component, here 2.5 μm (Acke et al. 2004), as shown for the warm dust component in Figure 13. We also explored less steep weighting, $\propto \lambda^{-0.3}$. An alternate approach is to use the disk component of the WMCRT code, as shown in Figure 14 to fit the SED at $\lambda \leqslant 10$ μm. For these models we used the Cotera et al. (2001) grains, in order to create a steep SED with a realistic grain model, yet having grains larger than a normal "interstellar" size distribution, in order to suppress the silicate emission band at 10 μm. Independent of the model, the steepness of the SED also implies that the range of grain temperatures is restricted to nearly a single temperature, suggesting that either the inner disk in the high-*J* state is actually a very narrow torus, or it is very optically thick immediately within its inner edge. In the latter case, it completely shadows more distant material, rendering it essentially invisible, as suggested by Fedele et al. (2008).

None of these models was fully capable of reproducing the steep drop-off in flux seen in the 1–10 μm region of the SED of SAO 206462. In particular, the Cotera et al. (2001) opacity model predicts strong silicate emission at 10 μm. Absence of silicate emission, as seen over the past 15 years (Coulson & Walther 1995; van Boekel et al. 2005; Meeus et al. 2001; Walker & Heinrichsen 2000; Kessler-Silacci et al. 2006), is usually interpreted in terms of grain growth, but this is also inconsistent with the steep wavelength dependence of the near to mid-IR SED, assuming cosmic abundances for carbon to silicates. Alternatively, Voshchinnikov & Henning (2008) note that the silicate emission can be suppressed in porous, aggregate grains by inclusion of amorphous carbon. Complete suppression of the 10 μm silicate emission, as indicated by the data, however, would imply an amorphous carbon content which is at the high end of the range inferred for other disks ($\geqslant$50%). Disk chemistry studies are still in their infancy, but departures from conventional disk composition have previously been noted for the Herbig Be star HD 100546, where the silicates are iron-poor (Malfait et al. 1998), and the infalling material is also iron-deficient (Grady et al. 1997). Carbon-rich dust has also been suggested for the disk of β Pictoris (Roberge et al. 2006), and for the debris belt of HR 4796 A (Debes et al. 2008), although an alternate chemistry was proposed by Köhler et al. (2008). Confirmation of a disk chemistry gradient in SAO 206462 will

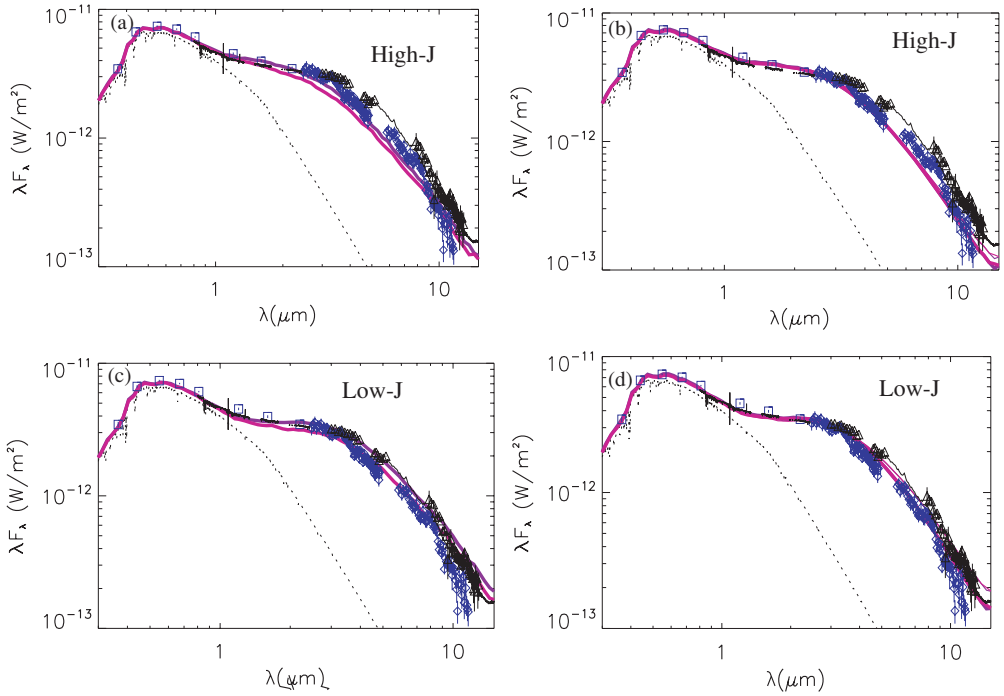

Figure 14. Modeling the inner disk of SAO 206462. (a) Fit to the high-*J* state using the Whitney code for inclinations of 10° (red) and 20° (purple), with a disk from 0.08 to 0.24 AU and the Cotera et al. (2001) opacity data. The fit is good to 3 μm but underestimates fluxes at $\lambda \gtrsim 3$ μm. (b) Fit to the high-*J* state using two different blackbodies: a $T = 1550$ K unweighted blackbody (thin) and a $T = 1400$ K blackbody weighted by $\lambda^{-0.3}$ (bold). (c) Fit to the low-*J* state using the Cotera et al. (2001) opacity data with a disk extending from 0.14 to 0.31 AU. The best fit inclination is 20°. (d) Comparison of the low-state data with an unweighted blackbody (thin line) of $T = 1300$ K and a $\lambda^{-0.3}$ weighted blackbody at $T = 1250$ K (thick line).

require a demonstration that the outer disk contains silicate grains, such as might be provided by PACS on *Herschel*, and also a demonstration that material reaching the star is deficient in silicate dissociation products, but rich in carbon, such as can be provided by high-resolution UV spectroscopy from *HST*.

Low J-band/high L-band state. In this state, the warm dust can be successfully fit with the WMCRT code using a disk model with the disk extending 0.14–0.31 AU and the Cotera et al. (2001) grain opacity model (Figure 13(c)) with the same lack of good fit near the 10 μm silicate feature in the *Spitzer* IRS data. Interestingly, the best-fit inclination of 20° is higher than either the 14° ± 3° inferred for warm CO (Pontoppidan et al. 2008) or the 11° ± 2° fitting the outer disk (Dent et al. 2005), but lower than the 60° inferred from 10 μm interferometry (Fedele et al. 2008). The $\lambda^{-0.3}$-weighted blackbody model also fits the disk in this state, albeit at a lower temperature (1200 K) than for the high *J* state, but provides no further geometrical or compositional insights.

4.5. Is SAO 206462 a Pre-Transitional Disk or a Young Planetary System?

The transition between a gap being opened in a disk, and the clearing of the entire inner dust disk is expected to be quick; observation of systems with wide gaps would be expected to be extremely rare (Varnière et al. 2006a, 2006b). A disk dominated by unprocessed (e.g., nonchemically fractionated) material, even with a large gap, should have the inner and outer dust disk components coplanar with each other and with the gas disk, and should show radially undifferentiated dust composition except for grain sublimation effects (e.g., a snow line). For a gapped disk, we would moreover expect that sublimation and carbon combustion would favor detection of silicates over carbonaceous material (Wehrstedt & Gail 2008) in the warm dust, since the sublimation temperatures are typically higher for silicates than for most organic compounds. The interferometric data (Fedele et al. 2008), and to a lesser extent, our SED fitting, together with the large fractional IR luminosity of the warm dust emission already suggest that the warm dust and outer disk components in the SAO 206462 system are not coplanar, suggesting that the inner disk has been significantly perturbed.

Planetesimal or planetary embryo collisions, however, can release copious amounts of small grains with composition traceable to their parent bodies rather than the bulk composition of the protoplanetary disk (Lisse et al. 2008). If confirmed by future observations, a reduced silicate abundance in the warm dust component of SAO 206462's disk would be consistent with it arising from the collisional erosion of carbon-rich parent bodies. In this case, the warm CO emission, which originates at radii from 0.2 to 10 AU may be a dissociation produce of such bodies, rather than an accretion by-product. Catastrophic collisions can also scatter material to large heights above the disk midplane, potentially accounting both for the unusually large fractional IR luminosity of the warm dust associated with SAO 206462, and for what may be a difference in inclination between the outer and inner disk. Small-grain debris from a single impact would be expected to have a lifetime in the inner disk of at most a few decades (Rhee et al. 2008), and should show a gradual evolution in the NIR excess light on timescales of weeks to months, if arising in a largely gas-free region. The NIR photometry for the warm dust component over the past 15 years suggests fluctuating emission, with significant changes in the SED on timescales as short as six weeks, rather than a simple monotonic decay as would be expected from a single, large impact. If supported by future observations, the presence of continued small grain production suggests that the inner disk

of SAO 206462 harbors a planetesimal belt, possibly similar to the inclined inner disk of β Pictoris (Heap et al. 2000), which itself appears to be associated with a mid-IR dust clump (Telesco et al. 2005), and what has been suggested to be a Jovian-mass planet candidate (Lagrange et al. 2009). The presence of such a belt in a system which has already been suggested to harbor one or more giant planets at larger distances from the star (Pontoppidan et al. 2008) strongly suggests that by 8 Myr, disks similar to SAO 206462 *are* young planetary systems. With its low inclination, this system is optimally suited for high contrast imaging searches for Jovian-mass planets.

This work, in part, is based on observations made with the NASA/ESA *Hubble Space Telescope*, obtained at the Space Telescope Science Institute, which is operated by the Association of Universities for Research in Astronomy, Inc., under NASA contract NAS 5-26555. These observations are associated with programs HST-GO-10177 and HST-GO-10864, but also made use of archival data from HST-GTO-7227, HST-GTO-8474, HST-GO-8674, HST 7858, HST-GO-9136, and CAL/STIS 8925. This study was also based on archival data obtained with the NASA-CNES-CSA *Far Ultraviolet Spectroscopic Explorer*. *FUSE* was operated for NASA by the Johns Hopkins University under NASA contract NAS5-32985. This work is based in part on data obtained with the *Spitzer Space Telescope*, which is operated by the Jet Propulsion Laboratory, California Institute of Technology under a contract with NASA. This work is also based in part on observations obtained at the Gemini Observatory, which is operated by the Association of Universities for Research in Astronomy, Inc., under a cooperative agreement with the NSF on behalf of the Gemini partnership: the National Science Foundation (United States), the Particle Physics and Astronomy Research Council (United Kingdom), the National Research Council (Canada), CONICYT (Chile), the Australian Research Council (Australia), CNPq (Brazil), and CONICET (Argentina). The Phoenix infrared spectrograph was developed and is operated by the National Optical Astronomy Observatory. C.A.G. is also supported as part of the Astrophysics Data Program under NASA contract NNH06CC28C to Eureka Scientific, HST-GO-10177.02-A, HST-GO-10864.01-A, through contract 1311495 issued by JPL/Caltech to Eureka Scientific. C.A.G. and K.H. are also supported by NASA's Astrobiology Institute (RTOP 344-53-51) to the Goddard Center for Astrobiology. G.S. is supported under HST-GO-10177.01. M.L.S. is supported through the NASA Origins of Solar Systems Program NAG5-9475 and NAG5-13242, and by NASA Astrophysics Data Program contracts NNH05CD30C and NASA NN09AC73G. K.A.C. is supported by a Kentucky Space Grant Consortium Fellowship under NASA National Space Grant College and Fellowship Program Grant NNG05GH07H. M.T. is supported under contract with the Jet Propulsion Laboratory (JPL) funded by NASA through the Michelson Fellowship Program. JPL is managed for NASA by the California Institute of Technology. This work was supported in part by The Aerospace Corporation's Independent Research and Development program. Data analysis facilities were provided by the Steward Observatory of the University of Arizona and the Astrophysical Systems Division at NASA's GSFC. We also thank the anonymous referee whose comments greatly improved the paper.

Facilities: HST (NICMOS), *HST* (STIS), *HST* (ACS), *FUSE*, *ROSAT*, *ISO* (ISOPHOT), *Spitzer Space Telescope* (IRS), *Spitzer Space Telescope* (MIPS), IRTF (SPeX), IRTF (BASS), Gemini-S (PHOENIX), Subaru

APPENDIX

ASSEMBLY OF THE IR SED

Assembly of a single SED for a Herbig star typically requires merging noncontemporaneous data sets taken with different instruments, using a range of apertures/slits and/or beam sizes. SAO 206462 is no exception, with IR data spanning 1983–2008, and including both the new observations discussed in Section 2, above, literature and previously unpublished archival data.

A.1. Optical and NIR Photometry

In the optical, SAO 206462 was observed by both Coulson & Walther (1995) and *Hipparcos* (Perryman et al. 1997) in the early 1990s. SAO 206462 was subsequently included in the Tycho catalog, and has a $\Delta V = 0\overset{m}{.}4$, suggestive of stellar activity, as expected for a mid-F star. The Coulson and Walther data and the Hale–Bopp photometry are both in the middle of the range observed by *Hipparcos*.

In the NIR, photometric observations for SAO 206462 include data from the early 1990s as part of Coulson & Walther (1995), 2MASS data from 2000 (Skrutskie et al. 2006), *HST*/NICMOS target acquisition photometry from 1998 and 2005, and Subaru CIAO data from 2008. The NICMOS data demonstrate significant variability (2.5σ even at the low S/N of the acquisition data) at 1.7 μm.

A.2. Cross-Calibration of the Spectrophotometry and Spectroscopy

Cross-calibration of IR spectrophotometry is essential to building a single SED for a star like SAO 206462. For an isolated, unresolved source, such as 47 UMa, the BASS spectrophotometry, ISO PHT40 and *Spitzer* IRS data agree to 5% in the NIR, with systematic differences at the 10%–20% level in the mid-IR (Figure 6(b)) for roughly contemporary observations of a single target (Figure 6(b)).

The *Spitzer* IRS data for SAO 206462 were obtained as part of a spectral map, so the data for SAO 206462 were not perfectly centered for any of the wavelength segments. The IRS low-resolution spectra here include four different slit sizes, one for the 5–15 μm low-resolution data and two other slits for the longer wavelength high-resolution data. All are roughly matched to the PSF of *Spitzer*. Thus, a fixed slit width produces more light loss at longer wavelengths than at shorter wavelengths, and is partially compensated for in the point-source calibration. We scaled the IRS 7–14 μm SL1 data up by 5% to match the BASS spectrophotometry in the same wavelength range for the full-blown SED modeling discussed in Section 4.4. The IRS 10–19 μm data required no additional scaling, but the 18–35 μm HL data were scaled down by 7% to match the HS data.

A.3. The FIR and Submillimeter data

At longer wavelengths, the SED of SAO 206462 is represented by *IRAS* photometry (Walker & Wolstencroft 1988; Beichman et al. 1988), *ISO* ISOPHOT photometry (Walker &

Table 3
Photometric and Spectrophotometric Data Used to Construct the SED

Data Set	λ(μm)	Aper. (″)	Mag.	Flux (Jy)	Date	Reference
	U	20	9.14	0.42 ± 0.02	1993 May 30	Coulson & Walther(1995)
	0.44	3.4		0.84 ± 0.03	2006 Aug 5	Hale–Bopp NB
	B	20	9.14	0.98 ± 0.02	1993 May 30	Coulson & Walther(1995)
Hipparcos	BT		9.228		1989–1993	Perryman et al. (1997)
	V	20	8.63	1.35 ± 0.02	1993 May 30	Coulson & Walther(1995)
	VT		8.46–8.80		1989–1993	Perryman et al. (1997)
	R	20	8.16	1.57 ± 0.02	1993 May 30	Coulson & Walther(1995)
	0.77	3.4		1.37 ± 0.03	2006 Aug 5	Hale–Bopp NB
	I	20	7.31	1.65 ± 0.02	1993 May 30	Coulson & Walther(1995)
	1.2	7.8	7.31	1.81 ± 0.04	1992 Apr 28	Coulson & Walther(1995)
2MASS	J	4	7.28 ± 0.03	1.95 ± 0.04	2000 Feb 4	Skrutskie et al. (2006)
CIAO	J	3.8	7.27 ± 0.02	1.93 Jy	2008 Jul 11	
	1.6	7.8	6.67	2.11 ± 0.05	1992 Apr 28	Coulson & Walther (1995)
2MASS	H	4	6.59 ± 0.03	2.42 ± 0.07	2000 Feb 4	Skrutskie et al. (2006)
NICMOS	1.7	1.58 × 1.58	6.48	2.426	1998 Aug 22	HST-GO-7857 visit 01
NICMOS	1.7	1.58 × 1.58	6.56	2.246	2005 Mar 24	HST-GO-10177 visit 39
NICMOS	1.7	1.58 × 1.58	6.55	2.274	2005 Mar 24	HST-GO-10177 visit 39a
	2.2	7.8	5.97	2.54 ± 0.10	1992 Apr 28	Coulson & Walther(1995)
2MASS	K	4	5.84 ± 0.02	3.06 ± 0.04	2000 Feb 4	Skrutskie et al. (2006)
	3.8	7.8	4.89	2.66 ± 0.10	1992 Apr 28	Coulson & Walther(1995)
CIAO	L'	3.0	4.87 ± 0.07	2.81 Jy	2008 Jul 11	
	4.75	7.8	4.54	2.34 ± 0.10	1992 Apr 28	Coulson &Walther(1995)
CIAO	M'	1.7	4.43 ± 0.09	2.76 Jy	2008 Jul 11	
IRAS	12	25		1.59 ± 0.10	1983 Nov	Walker & Wolstencroft(1988)
IRAS	25	25		6.71 ± 0.94	1983 Nov	Walker & Wolstencroft(1988)
KAO	47	∼ 25		24.3±3.5	1993–1994	Harvey et al. (1996)
IRAS	60	60		25.61 ± 3.59	1983 Nov	Walker & Wolstencroft(1988)
IRAS	100	100		25.69 ± 2.57	1983 Nov	Walker & Wolstencroft(1988)
ISOPHT	60	43.5 × 43.5		28.2 ± 4	1996 Feb 29	
ISOPHT	80	43.5 × 43.5		26 ± 4	1996 Feb 29	
ISOPHT	100	43.5 × 43.5		23 ± 4	1996 Feb 29	
ISOPHT	200	89.4 × 89.4		9.53	1996 Feb 29	Walker & Heinrichse(2000)
JCMT	350	19		5.8 ± 1.7	1992–1993	Coulson & Walther(1995)
	450	19		3.8 ± 1.5	1992–1993	”
	800	19		0.64 ± 0.04	1992–1993	”
	850	19		0.49 ± 0.01		Sandell & Weintraub(2002)
	1100	19		0.26 ± 0.04	1992–1993	Coulson & Walther(1995)
	1300	19		0.142 ± 0.042	1994 Aug	Sylvester et al. (1996)

Table 4
Spectral and Spectrophotometric Data Used to Construct the SED

Date	Obs. ID	Aperture (″)	λ(μm)	R	Reference
2003 Jun 9	*FUSE* Q3060201	30 × 30	0.091–0.119	20000	This study
2007 May 19	*HST* ACS PR130L	slitless	0.13–0.20		This study
2007 May 1	IRTF SpeX	0.8 × 15	0.8–5.4	2000	This study
2008 Jul 8	IRTF SpeX	0.8 × 15	0.8–2.4	2000	This study
2008 May 22	IRTF SpeX	0.8 × 15	0.8–5.4	2000	This study
2008 Mar 23	Gemini-S Phoenix	0.34	4.7	50000	This study
2007 Jul 9	IRTF/BASS	3.4	2.5–14	70	This study
1996 Feb 29	ISO PHT40 10401876	24 × 24	2.47–8.95	90	Walker & Heinrichsen (2000), Acke & van den Ancker (2004)
2004 Aug 8	*Spitzer* IRS LS	3.6 × 57	5.2–8.7	60–127	Sloan et al. (2005)
	Spitzer IRS LL	3.7 × 57	7.4–14.4	61–120	
	Spitzer IRS H	4.7 × 11.3	9.9–19.6	600	
2005 Feb 27	*Spitzer* MIPS SED	20 × 50	54–98	15–25	Brown et al. (2007)

Heinrichsen 2000), KAO 47 μm photometry (Harvey et al. 1996), and *Spitzer* IRS and MIPS SED data, as well as submillimeter and millimeter observations from the literature. The ISOPHOT, KAO, *IRAS*, and MIPS data show good agreement with each other, to within calibration uncertainties in the literature, despite the larger beam sizes used for some observations (Table 3). The agreement of these data indicates minimal galactic cirrus contamination of the SAO 206462 data. In the FIR, the *ISO* ISOPHOT and the submillimeter data from Coulson & Walther (1995) and Sylvester et al. (1996) show monotonically decreasing λF_λ with increasing wavelength, as expected for a circumstellar disk: we adopt them without any need for scaling.

Table A1
Photometric Variability of SAO 206462

λ (μm)	Minimum Flux (Jy)	Maximum Flux (Jy)	% Variation
0.8	1.47 (SpeX)	1.68 (Coulson and Williams)	13%
J	1.67 (SpeX)	1.98 (2MASS)	16%
H	1.98 (SpeX)	2.42 (NICMOS/F171M)	22%
K:	2.49 (Coulson & Williams)	3.12 (2MASS)	16%
3.75	1.84 (ISO PHT40, SpeX,Subaru)	2.16 (BASS)	16%
4.75	2.69 (SpeX, ISO PHT40)	3.17 (BASS, *Spitzer*-IRS, extrapolated)	16%
10.0	0.7 (ISO PHT40)	1.3 (BASS/*Spitzer*-IRS)	60%

A.4. IR Variability of SAO 206462

The flux range as a function of wavelength for SAO 206462 is shown in Table A1. At wavelengths shortward of 4.75 μm, at least 13%–16% variations are present, corresponding to 3σ detections of variability. At wavelengths where the temporal coverage is better, larger ranges are observed, suggesting that the existing data, while demonstrating variability, do not sample the full amplitude of variation. The most striking range is seen at 10 μm, where we find 60% variations, corresponding to 4σ.

REFERENCES

Acke, B., & van den Ancker, M. E. 2004, A&A, 426, 151
Acke, B., van den Ancker, M. E., Dullemond, C. P., van Boekel, R., & Waters, L. B. F. M. 2004, A&A, 422, 621
Ardila, D. R., Golimowski, D. A., Krist, J. E., Clampin, M., Ford, H. C., & Illingworth, G. D. 2007, ApJ, 665, 512
Aufdenberg, J. P., et al. 2006, ApJ, 645, 664
Augereau, J.-C., Lagrange, A. M., Mouillet, D., & Ménard, F. 2001, A&A, 365, 78
Baines, D., Oudmaijer, R. D., Porter, J. M., & Pozzo, M. 2006, MNRAS, 367, 737
Beichman, C., Nugebauer, G., Habing, H. J., Clegg, P. E., & Chester, T. J. 1988, *Infrared Astronomical Satellite* (*IRAS*) Catalogs and Atlases, Vol. 1, Explanatory Supplement (Washington, DC: NASA)
Berghöfer, T. W., Schmitt, J. H. M. M., & Hünsch, M. 1999, A&A, 342, L17
Brittain, S., Najita, J., & Carr, J. 2009, ApJ, submitted
Brittain, S. D., Rettig, T. W., Simon, T., Kulesa, C., DiSanti, M. A., & Dello Russo, N. 2003, ApJ, 588, 535
Brittain, S. D., Simon, T., Najita, J. R., & Rettig, T. W. 2007, ApJ, 659, 685
Brown, J. M., et al. 2007, ApJ, 664, L107
Carciofi, A. C., Domiciano de Souza, A., Magalhães, A. M., Bjorkman, J. E., & Vakili, F. 2008, ApJ, 676, L41
Chiang, E., & Goldreich, P. 1997, ApJ, 490, 368
Chiang, E., & Goldreich, P. 1999, ApJ, 519, 279
Collins, K. A., Grady, C. A., Woodgate, B., & Williger, G. M. 2007, Detection of Optical Ghost in the *HST* ACS Solar Blind Channel Filter F122M, Instrument Science Report, ACS 2007-005 (Baltimore, MD: STScI)
Cotera, A. S., et al. 2001, ApJ, 556, 958
Coulson, I. M., & Walther, D. M. 1995, MNRAS, 274, 977
Cushing, M. C., Vacca, W. D., & Rayner, J. T. 2004, PASP, 116, 362
de la Reza, R., & Pinzón, G. 2004, AJ, 128, 1812
Debes, J. H., Weinberger, A. J., & Schneider, G. 2008, ApJ, 673, L191
Deleuil, M., et al. 2005, A&A, 429, 247
Dent, W. R. F., Greaves, J. S., & Coulson, I. M. 2005, MNRAS, 359, 663
Devine, D., Grady, C. A., Kimble, R. A., Woodgate, B., Bruhweiler, F. C., Boggess, A., Linsky, J. L., & Clampin, M. 2000, ApJ, 542, L115
Dixon, W. V., et al. 2007, PASP, 119, 527
Doering, R. L., Meixner, M., Holfeltz, S. T., Krist, J. E., Ardila, D. R., Kamp, I., Clampin, M. C., & Lubow, S. H. 2007, AJ, 133, 2122
Domiciano de Souza, A., Kervella, P., Jankov, S., Abe, L., Vakili, F., di Folco, E., & Paresce, F. 2003, A&A, 407, L47 (D03)
Dominik, C., Dullemond, C. P., Waters, L. B. F. M., & Walch, S. 2003, A&A, 398, 607
Doucet, C., Pantin, E., Lagage, P. O., & Dullemond, C. P. 2006, A&A, 460, 117
Dullemond, C. P., & Dominik, C. 2004a, A&A, 417, 159
Dullemond, C. P., & Dominik, C. 2004b, A&A, 421, 1075
Dunkin, S. K., Barlow, M. J., & Ryan, S. G. 1997a, MNRAS, 286, 604
Dunkin, S. K., Barlow, M. J., & Ryan, S. G. 1997b, MNRAS, 290, 165
Dupree, A., Brickhouse, N. S., Smith, G. H., & Strader, J. 2005, ApJ, 625, L131
Farnham, T. L., Schleicher, D. G., & A'Hearn, M. F. 2000, Icarus, 147, 180
Fedele, D., et al. 2008, A&A, 491, 809
Furlan, E., et al. 2005, ApJ, 628, L65
Garcia Lopez, R., Natta, A., Testi, L., & Habart, E. 2006, A&A, 459, 837
Geers, V. C., et al. 2006, A&A, 459, 545
Gerbaldi, M., Faraggiana, R., Burnage, R., Delmas, F., Gómez, A. E., & Grenier, S. 1999, A&AS, 137, 273
Gordon, K. G., et al. 2005, PASP, 117, 503
Grady, C. A., Sitko, M. L., Bjorkman, K. S., Pérez, M. R., Lynch, D. K., Russell, R. W., & Hanner, M. S. 1997, ApJ, 483, 449
Grady, C. A., et al. 2000, ApJ, 544, 895
Grady, C. A., et al. 2001, AJ, 122, 3396
Grady, C. A., et al. 2004, ApJ, 608, 809
Grady, C. A., et al. 2005, ApJ, 630, 958
Grady, C. A., et al. 2007, ApJ, 665, 1391
Guimarães, M. M., Alencar, S. H. P., Corradi, W. J. B., & Vieira, S. L. A. 2006, A&A, 457, 581
Hamaguchi, K., Yamauchi, S., & Koyama, K. 2005, ApJ, 618, 360
Harper, G. M., Wilkinson, E., Brown, A., Jordan, C., & Linsky, J. L. 2001, ApJ, 551, 486
Harvey, P. M., Smith, B. J., Difrancesco, J., Colome, C., & Low, F. J. 1996, ApJ, 471, 973
Heap, S. R., Lindler, D. J., Lanz, T. M., Cornett, R. H., Hubeny, I., Maran, S. P., & Woodgate, B. 2000, ApJ, 539, 435
Hinkle, K. H., Cuberly, R. W., Gaughan, N. A., Heynssens, J. B., Joyce, R. R., Ridgway, S. T., Schmitt, P., & Simmons, J. E. 1998, Proc. SPIE, 3354, 810
Hinkle, K. H., Joyce, R. R., Sharp, N., & Valenti, J. A. 2000, Proc. SPIE, 4008, 720
Hinkle, K. H., et al. 2003, Proc. SPIE, 4834, 353
Hog, E., Kuzmin, A., Bastian, U., Fabricius, C., Kuimov, K., Lindegren, L., Makarov, V. V., & Roeser, S. 1998, A&A, 335, L65
Juhász, A., Prusti, T., Ábrahám, P., & Dullemond, C. P. 2007, MNRAS, 374, 1242
Jura, M., Malkan, M., White, R., Telesco, C., Piña, R., & Fisher, R. S. 1998, ApJ, 505, 897
Kessler-Silacci, J., et al. 2006, ApJ, 639, 275
Kim, S. H., Martin, P. G., & Hendry, P. D. 1994, ApJ, 422, 164
Köhler, M., Mann, I., & Li, A. 2008, ApJ, 686, 95
Kurucz, R. 1993, Kurucz CD-ROM No. 13, ATLAS9 Stellar Atmosphere Programs and 2 km s^{-1} Grid (Cambridge: SAO)
Kwan, J., Edwards, S., & Fischer, W. 2007, ApJ, 657, 897
Lagrange, A.-M., et al. 2009, A&A, 493, L21
Lallement, R., Welsh, B. Y., Vergely, J. L., Crifo, F., & Sfeir, D. 2003, A&A, 411, 447
Leggett, S. K., et al. 2002, ApJ, 564, 452
Leggett, S. K., et al. 2003, MNRAS, 345, 144
Leggett, S. K., et al. 2006, MNRAS, 373, 781
Lisse, C., Chen, C. H., Wyatt, M. C., & Morlok, A. 2008, ApJ, 673, 1106
Lowrance, P. J., et al. 1999, ApJ, 512, L69
Lu, N., et al. 2008, PASP, 120, 328
Malfait, K., Waelkens, C., Waters, L. B. F. M., Vandenbussche, B., Huygen, E., & de Graauw, M. S. 1998, A&A, 332, L25
Martin-Zaïdi, C., et al. 2008, A&A, 484, 225
Meeus, G., Waters, L. B. F. M., Bouwman, J., van den Ancker, M. E., Waelkens, C., & Malfait, K. 2001, A&A, 365, 476
Murakawa, K., et al. 2004, PASJ, 56, 509
Najita, J., Carr, J. S., & Mathieu, R. D. 2003, ApJ, 589, 931
Najita, J. R., Strom, S. E., & Muzerolle, J. 2007, MNRAS, 378, 369
Oudmaijer, R., van der Veen, W. E. C. J., Waters, L. B. F. M., Trams, N. R., Waelkens, C., & Engelsman, E. 1992, A&AS, 96, 625, http://www.stsci.edu/hst/acs/

Pavlovsky, C., Koekemoer, A., & Mack, J. 2006, ACS Data Handbook, Vol. 5.0, ed. D. Karakla & S. Rose (Baltimore, MD: STScI)
Perryman, M. A. C., et al. 1997, A&A, 323, L49
Peterson, D. M., et al. 2006a, ApJ, 636, 1087
Peterson, D. M., et al. 2006b, Nature, 440, 896
Pontoppidan, K. M., Blake, G. A., van Dishoeck, E. F., Smette, A., Ireland, M. J., & Brown, J. 2008, ApJ, 684, 1323
Qi, C., et al. 2004, ApJ, 616, L11
Rayner, J. T., Toomey, D. W., Onaka, P. M., Denault, A. J., Stahlberger, W. E., Vacca, W. D., Cushing, M. C., & Wang, S. 2000, PASP, 115, 362
Redfield, S., Linsky, J. L., Ake, T. B., Ayres, T. R., Dupree, A. K., Robinson, R. D., Wood, B. E., & Young, P. R. 2002, ApJ, 581, 626
Rhee, J. H., Song, I., & Zuckerman, B. 2008, ApJ, 675, 777
Rieke, G. H., et al. 2004, ApJS, 154, 25
Roberge, A., Feldman, P. D., Weinberger, A. J., Deleuil, M., & Bouret, J.-C. 2006, Nature, 441, 724
Roberge, A., et al. 2001, ApJ, 551, L97
Robitaille, T. P., Whitney, B. A., Indebetouw, R., & Wood, K. 2007, ApJS, 169, 328
Roesser, S., & Bastian, U. 1988, A&AS, 74, 449
Sasseen, T. P., Hurwitz, M., Dixon, W. V., & Airieau, S. 2002, ApJ, 566, 267
Schneider, G., Sliverstone, M. D., & Hines, D. C. 2005, ApJ, 629, L117
Schneider, G., Weinberger, A. J., Becklin, E. E., Debes, J. H., & Smith, B. A. 2009, AJ, 137, 53
Schneider, G., et al. 2003, AJ, 125, 1467
Schneider, G., et al. 2006, ApJ, 650, 414
Simon, T., Ayres, T. R., Redfield, S., & Linsky, J. L. 2002, ApJ, 579, 800
Sitko, M. L., et al. 2008, ApJ, 678, 1070
Skinner, S. L., Güdel, M., Audard, M., & Smith, K. 2004, ApJ, 614, 221
Skrutskie, M. F., et al. 2006, AJ, 131, 1163
Sloan, G. C., et al. 2005, ApJ, 632, 956
Stelzer, B., Huélamo, N., Micela, G., & Hubrig, S. 2006, A&A, 452, 1001
Strom, S. E., Edwards, S., & Strom, K. M. 1989, in Proc. The Formation and Evolution of Planetary Systems, Constraints on the Properties and Environment of Primitive Stellar Nebulae from the Astrophysical Record Provided by Young Stellar Objects, ed. H. A. Weaver & L. Danly (Cambridge: Cambridge Univ. Press), 91–106
Sylvester, R. J., Skinner, C. J., Barlow, M. J., & Mannings, V. 1996, MNRAS, 279, 915
Telesco, C. M., et al. 2005, Nature, 433, 133
Thamm, E., Steinacker, J., & Henning, Th. 1994, A&A, 287, 493
Thi, W.-F., et al. 2001, ApJ, 561, 1074
Tokunaga, A. T., & Vacca, W. D. 2005, PASP, 117, 42
Tsuboi, Y., Maeda, Y., Feigelson, E. D., Garmire, G. P., Chartas, G., Mori, K., & Pravdo, S. H. 2003, ApJ, 587, L51
Vacca, W. D., Cushing, M. C., & Rayner, J. T. 2003, PASP, 115, 389
van Boekel, R., Min, M., Waters, L. B. F. M., de Koter, A., Dominik, C., van den Ancker, M. E., & Bouwman, J. 2005, A&A, 437, 189
van der Plas, G., van den Ancker, M. E., Fedele, D., Acke, B., Dominik, C., Waters, L. B. F. M., & Bouwman, J. 2008, A&A, 485, 487
Varniére, P., Bjorkman, J. E., Frank, A., Quillen, A. C., Carciofi, A. C., Whitney, B. A., & Wood, K. 2006a, ApJ, 637, L125
Varniére, P., Blackman, E. G., Frank, A., & Quillen, A. C. 2006b, ApJ, 640, 1110
Voshchinnikov, N. V., & Henning, Th. 2008, A&A, 483, L9
Walker, H. J., & Heinrichsen, I. 2000, Icarus, 143, 147
Walker, H. J., & Wolstencroft, R. D. 1988, PASP, 100, 1509
Wassell, E. J., Grady, C. A., Woodgate, B., Kimble, R. A., & Bruhweiler, F. C. 2006, ApJ, 650, 985
Wehrstedt, M., & Gail, H.-P. 2008, A&A, in press (arXiv:0804.3377)
Werner, M. W., et al. 2004, ApJS, 154, 1
Whitney, B. A., Indebetouw, R., Bjorkman, J. E., & Wood, K. 2004, ApJ, 617, 1177
Whitney, B. A., Wood, K., Bjorkman, J. E., & Cohen, M. 2003a, ApJ, 598, 1079
Whitney, B. A., Wood, K., Bjorkman, J. E., & Wolff, M. J. 2003b, ApJ, 591, 1049
Wisniewski, J. P., Clampin, M., Grady, C. A., Ardila, D. R., Ford, H. C., Golimowski, D. A., Illingworth, G. D., & Krist, J. E. 2008, ApJ, 82, 548
Wood, K., Wolff, M. J., Bjorkman, J. E., & Whitney, B. A. 2002, ApJ, 564, 887